A numerical approach for hydrodynamic performance evaluation of multi-degree-of-freedom floating oscillating water column (OWC) devices

Cong, Peiwen
State Key Laboratory of Coastal and Offshore Engineering, Dalian University of Technology

Teng, Bin
State Key Laboratory of Coastal and Offshore Engineering, Dalian University of Technology

Liu, Yingyi
Research Institute for Applied Mechanics, Kyushu University

Ning, Dezhi
State Key Laboratory of Coastal and Offshore Engineering, Dalian University of Technology

出版情報：Journal of Fluids and Structures. 114, pp.103730-, 2022-10. Elsevier
バージョン：
権利関係：

A numerical approach for hydrodynamic performance evaluation of multi-degree-of-freedom floating oscillating water column (OWC) devices

Authors and affiliations:

Peiwen Cong[a*], Bin Teng[a], Yingyi Liu[b], Dezhi Ning[a]

[a.] *State Key Laboratory of Coastal and Offshore Engineering, Dalian University of Technology, Dalian 116024, China*

[b.] *Research Institute for Applied Mechanics, Kyushu University, Fukuoka 8168580, Japan*

[*] Corresponding Author

E-mail addresses:

Peiwen Cong pwcong@dlut.edu.cn

Bin Teng bteng@dlut.edu.cn

Yingyi Liu liuyingyi@riam.kyushu-u.ac.jp

Dezhi Ning dzning@dlut.edu.cn

A numerical approach for hydrodynamic performance evaluation of multi-degree-of-freedom floating oscillating water column (OWC) devices

Abstract

A numerical approach has been developed in this study for hydrodynamic analysis of complex-shaped oscillating water column (OWC) converters. Physically, in the circumstance when the device is free to move or moored in waves, the airflow movement inside the chamber is coupled tightly with the changing of the internal fluid surface and the hydrodynamic response of the device. By taking these coupling effects into account, appropriate boundary integral equations are formulated with supplemental theoretical relations. The boundary value problem is then solved using a higher-order boundary element method (HOBEM). After obtaining the wave force and dynamic air force, the coupled motions and hydrodynamic efficiency are evaluated by integration. In particular, unlike the conventional methods limited to fixed OWCs, the proposed method is proved applicable to those floating with coupled rigid-body motions. An optimal turbine parameter is hence mathematically derived to maximise the wave power absorption. Besides the linear quantities, nonlinear wave drift loads are evaluated via a newly derived formulation that accounts for the far-field contribution and the oscillating air pressure over the internal fluid surface. Based on the above methodology and the resulting tool, numerical studies are carried out for three cylindrical OWC scenarios that are floating in waves, attached by a reflector and connected to a submerged caisson, respectively. Different modes of body motion and typical free-surface oscillation modes in the chamber are analysed and discussed. It is found that, for an OWC with an attached arc-shaped reflector or connected to a submerged caisson, its wave power absorption can be characterised by a series of apparent peaks which are associated with the resonant internal fluid and in close proximity to the resonance frequencies of body motions involving surge, heave or pitch. Numerical results also indicate the benefits of floating OWCs from the coupled rigid-body motion modes and OWC's resonance,

expanding the frequency range of efficient conversion and improving the device's adaptability to variable oceanic environments.

Keywords: OWC; wave power absorption; wave drift force; HOBEM; BBDB

1. Introduction

A global energy transition away from fossil fuels to low-carbon solutions is in urgent need due to limited resources of fossil fuels, let alone its pollutant nature. This energy transition is made possible by technological innovations, notably in the field of renewable energy (Gielen, et al., 2019). Renewable energy techniques are steadily gaining importance worldwide. Since the ocean is vast with huge territories and full of ocean waves containing tremendous energy, wave energy is commonly recognised as a significant potential renewable energy resource (Cruz, 2008).

Considerable efforts have been made in the exploitation of wave energy. A number of wave energy converters have been designed and put into practice. Of the numerous devices devised for converting the wave energy, one that particularly stands out is the oscillating water column (OWC) device (Falcão, 2010). OWCs have been designed for different purposes, such as wave energy extraction and motion reduction of floating platforms, adaptable over a range of collector forms either situated on the coastline or floating offshore (Heath, 2012). The operating environment of an onshore OWC usually is safe, and mooring lines and submarine power cables are not requisite. Due to these apparent survival advantages, onshore OWCs have received much attention among researchers (Luo et al., 2014a; Vyzikas et al., 2017; Zhu et al., 2020; Wang et al., 2021). Integrating an OWC into a breakwater for coastal or harbour protection can probably be an easy solution for onshore OWCs, from economic, constructional, and operational points of view. The performance of OWCs integrated into a breakwater has been studied in many works (He et al., 2013; He et al., 2017; Zheng et al., 2019; Zhao et al., 2021). In addition, to improve the adaptability of OWCs, some innovative configurations, such as the multi-chamber OWC, OWC array, and the combination of OWC with offshore platform or wind turbine foundation, have been reported by researchers (Nader et al.,

2012; Nihous, 2012; Rezanejad et al., 2015; Ning et al., 2018; Zheng et al., 2018; Michele et al., 2019; Gadelho et al., 2021; Cong et al., 2021).

As waves approach a shoreline, the wave motion can be affected by the seabed, which can cause a reduction of wave height. A shoreline location also introduces limitations to deploying a large number of OWCs. Therefore, offshore OWCs, placed at higher wave energy sites, have been recommended and designed in many studies (Evans and Porter, 1997; Vijayakrishna Rapaka et al., 2004; Gomes et al., 2012; Elhanafi et al., 2017). Offshore OWCs are generally floating devices, having a typical geometry as a truncated column with an open bottom. The operational principle of an OWC moving in waves resembles that of a stationary one but differs in some aspects. The main difference lies in that the airflow within the chamber depends on not only the oscillation of the internal free surface but also the motion of the device. Currently, the performance of moving OWCs has been concerned in some studies. Hong et al. (2004) developed a numerical model based on the potential matching at the common surface separating the inner and outer domains and studied the body motions of floating OWCs. Luo et al. (2014b) studied a two-dimensional heaving OWC device based on numerical wave tank technology, and discovered the magnificent power capture efficiency around the natural frequency of heave motion. The coupling effects between the heave motion and the piston-mode fluid motion in the chamber have been examined by Gomes et al. (2016) with a spar-buoy wave energy converter and Sheng (2019) with a backward bent duct buoy (BBDB) OWC, respectively, using a two-rigid-body model, in which the water body in the water column is represented by an 'imaginary piston'. To broaden the effective frequency bandwidth, Wang et al. (2019) proposed a novel system consisting of a heave-only offshore OWC and an onshore unit.

The present study aims to provide an efficient and reliable numerical approach for the hydrodynamic analysis of arbitrarily shaped three-dimensional floating OWCs. A number of quadratic elements have been used to define the internal free surface, which allows the calculation of the free-surface fluctuations within the chamber as well as the hydrodynamic parameters relating to the oscillating air pressure. In conjunction with a higher-order boundary element method (HOBEM), appropriate boundary integral

equations are derived for the numerical model. The model is capable of carrying out various analyses for OWCs, including the hydrodynamic coefficients, wave force, free-surface elevation, motion response, and wave power absorption. An optimal turbine parameter with which the maximum wave power absorption can be attained is derived for multi-degree-of-freedom OWCs. In addition, besides the linear wave exciting force and wave radiation force (expressed in terms of added mass and radiation damping), the mean wave drift wave force on OWCs, caused by the weakly-nonlinear wave-body interaction, is also calculated. The mean wave drift force is of the second order with respect to wave steepness and is generally small in magnitude compared with the linear oscillatory part. However, it may cause large body excursions from its mean position when the restoring force is weak. In this study, a novel formulation of the mean wave drift force on OWCs is derived based on momentum conservation. The derived formulation consists of a term contributed by quantities at the far-field and a term associated with the oscillating air pressure within the chamber. Based on the developed numerical approach, detailed numerical studies are conducted for various scenarios. The hydrodynamic performance of three multi-degree-of-freedom cylindrical OWCs, floating in waves, attached by a reflector or connected to a submerged caisson, are discussed respectively.

The remaining part is organised as follows. Section 2 introduces the fundamental mathematical theory for a floating OWC, summarising the preceding works so far. Section 3 presents a novel HOBEM solution to the problem, followed by evaluating the resultant body motion and wave power absorption in Section 4. The optimal turbine parameter for a given sea state is mathematically derived in Section 5. Computation of the mean wave drift force upon OWCs based on momentum conservation is introduced in Section 6. A series of numerical analyses are performed in Section 7. Finally, conclusions are summarised in Section 8.

2. Hydrodynamic problem and power take-off model

The wave interaction with a floating OWC is concerned in this study. The device is allowed to flow in its six degrees of freedom in waves, and a description of this problem

is shown in Fig. 1. In Fig. 1, S_b, S_f, and S_p are respectively the body surface, the free surface, and the internal surface of the air chamber in calm water, while S_B, S_F, and S_P respectively represent the instantaneous surfaces. As shown in Fig. 1, two coordinate systems are used in the analysis. *Oxyz* is a space-fixed coordinate system with $z = 0$ the undisturbed position of the free surface and the z-axis positive upwards. $O'x'y'z'$ is a body-fixed coordinate system. In calm water, *Oxyz* and $O'x'y'z'$ coincide with each other. The fluid is assumed to be inviscid and incompressible, and the velocity field is irrotational. Then, the fluid velocity can be represented by the gradient of the velocity potential Φ satisfying Laplace's equation. When the space-fixed coordinate system is adopted, the governing equation is

$$\nabla^2\Phi(\mathbf{x};\ t)=0, \tag{1}$$

where $\mathbf{x} = (x, y, z)^T$ is the position vector in the space-fixed coordinate system; t is the time. The device is exposed to the action of monochromatic incident waves of small amplitude A and frequency ω. With the employment of the linear wave theory, the frequency-domain analysis is conducted. Then, the velocity potential can be expressed as

$$\Phi(\mathbf{x};\ t)=\mathrm{Re}\left[\phi(\mathbf{x})e^{-\mathrm{i}\omega t}\right], \tag{2}$$

where 'Re' indicates that the real part is to be taken; i is the imaginary unit; $\phi(\mathbf{x})$ is the spatial potential.

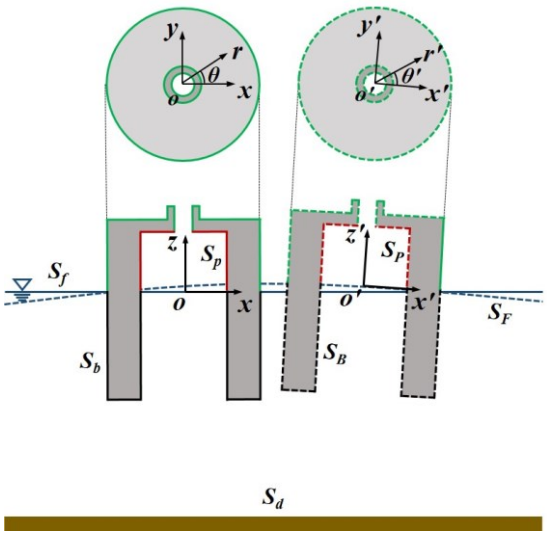

Fig. 1 Sketch of wave interaction with a floating OWC device and the definition of coordinate

systems

Besides Laplace's equation, appropriate boundary conditions should be satisfied by the potential. Outside the chamber, there is only the atmospheric pressure P_0 on the free surface. However, within the chamber, the free surface is subjected to the air pressure $P_0 + P_c(t)$, with $P_c(t)$ being the oscillating air pressure. Following Evans and Porter (1997) and Martins-Rivas and Mei (2009), the oscillating air pressure is assumed to be spatially uniform throughout the chamber. Referring to Sarmento and Falcão (1985), the following relationship is held for a linear turbine:

$$\frac{\mathrm{d}M_a}{\mathrm{d}t} = \rho_a Q_c - \frac{V_0}{c^2}\frac{\mathrm{d}P_c}{\mathrm{d}t} = \frac{KD}{N}P_c, \tag{3}$$

where M_a is the mass of the air in the chamber; Q_c is the change rate of the air volume; V_0 is the volume of the air in the chamber in still water; ρ_a is the air density; D is the diameter of the turbine rotor; N is the rotational speed of turbine blades; c is the speed of sound in the air; the empirical coefficient K depends on the design of the turbine. When the device is free to move or moored in waves, the air volume V_c depends on both the movement of the internal free surface S_i and the motion of the device. Then, the volume flux Q_c can be expressed as

$$Q_c = -\frac{\mathrm{d}\Delta V_c}{\mathrm{d}t}, \tag{4}$$

where

$$\Delta V_c = \iint_{S_i} \left\{ \left[\Xi_3 + \Xi_4 \cdot (y - y_o) - \Xi_5 \cdot (x - x_o) \right] - \zeta \right\} \mathrm{d}s. \tag{5}$$

In Eq. (5), ζ is the free-surface elevation within the chamber; Ξ_3, Ξ_4 and Ξ_5 denote the heave, roll and pitch displacements of the device, respectively. The rotation centre $\mathbf{x}_o$ is located at (0, 0, 0) in this study. For simple harmonic motions with

$$Q_c(t) = \mathrm{Re}\left[q_c e^{-\mathrm{i}\omega t} \right]; \tag{6a}$$

$$P_c(t) = \mathrm{Re}\left[p_c e^{-\mathrm{i}\omega t} \right]; \tag{6b}$$

$$\Xi_j(t) = \mathrm{Re}\left[\xi_j e^{-\mathrm{i}\omega t} \right], \quad (j = 1,\ 2,\ \ldots,\ 6); \tag{6c}$$

$$\zeta(x,\ y,\ t) = \mathrm{Re}\left[\eta e^{-\mathrm{i}\omega t}\right], \tag{6d}$$

where Ξ_1, Ξ_2 and Ξ_6 denote the surge, sway and yaw displacements; q_c, p_c, ξ_j and η are the complex amplitudes of the quantities, we can have

$$p_c = \Lambda q_c. \tag{7}$$

In Eq. (7), Λ is the pneumatic damping coefficient for the energy extraction of the air turbine, and it is expressed as

$$\Lambda = \left(\chi - \mathrm{i}\omega\mu\right)^{-1}, \tag{8}$$

with

$$\chi = \frac{KD}{N\rho_a}; \tag{9a}$$

$$\mu = \frac{V_0}{c^2\rho_a}. \tag{9b}$$

In Eq. (9), the parameters χ and μ depend on the design of the air turbine and air chamber, respectively. Hereinafter, they are referred to as the turbine parameter and chamber parameter, respectively.

The boundary conditions on instantaneous body surface S_B and free surface S_F are not convenient for direct use. When the amplitudes of body motion and wave motion are small, the boundary conditions can be satisfied on the mean body surface S_b and the still free surface S_f by performing Taylor series expansions. Then, according to Evans and Porter (1997), the following boundary condition is held by the total complex potential ϕ on the mean free surface ($z = 0$):

$$\frac{\partial\phi}{\partial z} - \frac{\omega^2}{g}\phi = \frac{\mathrm{i}\omega}{\rho g} p_c, \quad \text{on } S_i; \tag{10a}$$

$$\frac{\partial\phi}{\partial z} - \frac{\omega^2}{g}\phi = 0, \quad \text{on } S_e. \tag{10b}$$

In Eq. (10a), the effect of oscillating air pressure has been taken into account over the internal free surface S_i. In Eq. (10b), S_e is the portion of the free surface outside the chamber.

On the impermeable body surface, the boundary condition is given by

$$\frac{\partial \phi}{\partial n} = -\mathrm{i}\omega \sum_{j=1}^{6} \left(\xi_j n_j \right), \quad \text{on } S_b, \tag{11}$$

where $\mathbf{n} = (n_x, n_y, n_z)^T = (n_1, n_2, n_3)^T$ is the normal vector on S_b; $(n_4, n_5, n_6)^T = (\mathbf{x} - \mathbf{x}_o) \times \mathbf{n}$. In the same way, the boundary condition on the impermeable sea bed is

$$\frac{\partial \phi}{\partial z} = 0, \quad \text{on } z = -h. \tag{12}$$

For the sake of solution uniqueness, the Sommerfeld condition is employed as the far-field condition. That is

$$\lim_{r \to \infty} \sqrt{r} \left[\frac{\partial}{\partial r} \left(\phi - \phi_I \right) - \mathrm{i}\kappa_0 \left(\phi - \phi_I \right) \right] = 0, \tag{13}$$

With−

$$\phi_I \left(\mathbf{x} \right) = -\frac{\mathrm{i}Ag}{\omega} \frac{\cosh\left[\kappa_0 \left(z + h \right) \right]}{\cosh\left(\kappa_0 h \right)} \mathrm{e}^{\mathrm{i}\kappa_0 \left(x\cos\beta + y\sin\beta \right)}. \tag{14}$$

In Eqs. (13) and (14), $\phi_I \left(\mathbf{x} \right)$ is the incident potential; κ_0 is the wavenumber; β is the wave heading. κ_0 and ω satisfy the dispersion relation $\omega^2 = g\kappa_0 \tanh\left(\kappa_0 h \right)$, with g being the gravitational acceleration.

The extracted wave power W_c is defined by the time-averaged rate of work done by the chamber pressure pushing air through the turbine (Falcão and Henriques, 2016). W_c can be evaluated according to

$$W_c = \lim_{\hat{T} \to \infty} \left\{ \frac{1}{\hat{T}} \int_{t}^{t+\hat{T}} P_c \left(t \right) Q_c \left(t \right) \mathrm{d}t \right\}. \tag{15}$$

For regular incident waves, W_c can be further expressed as

$$W_c = \frac{1}{2} \mathrm{Re}\left[p_c q_c^* \right] = \frac{1}{2} \chi \left| p_c \right|^2. \tag{16}$$

3. A HOBEM model for the boundary value problem

In order to find the solution to the boundary value problem defined in the preceding sections, we decompose the total air volume flux into three distinct parts. That is

$$q_c = \hat{q} - \mathrm{i}\omega \sum_{j=1}^{6} \left(\xi_j q_j \right) - \frac{\mathrm{i}\omega}{\rho g} p_c q_R, \tag{17}$$

in which $\hat{q}$ is contributed by the incident and diffracted waves; q_j (j = 1, 2, …, 6) is the volume flux induced by the body motion of the jth oscillatory mode without the effects of incident waves and the oscillating air pressure; q_R represents that in a pressure-dependent wave radiation problem.

Correspondingly, the following decomposition can be made for the velocity potential:

$$\phi = \hat{\phi} - \mathrm{i}\omega \sum_{j=1}^{6} \left(\xi_j \phi_j \right) - \frac{\mathrm{i}\omega}{\rho g} p_c \phi_R, \tag{18}$$

where $\hat{\phi} = \phi_I + \phi_D$ represents a summation of the incident potential ϕ_I and the diffraction potential ϕ_D; ξ_j is the amplitude for the jth motion mode of the device ; ϕ_j is the radiation potential due to the jth mode rigid-body motion of unit amplitude; ϕ_R is the radiation potential induced by the oscillating air pressure of unit amplitude. ϕ_D, ϕ_j and ϕ_R all satisfy Laplace's equation, a no-flow condition on the seabed, and the Sommerfeld radiation condition. On the free surface, the following conditions are satisfied by ϕ_D, ϕ_j and ϕ_R:

$$\frac{\partial \phi_D}{\partial z} - \frac{\omega^2}{g} \phi_D = 0, \quad \text{on } S_i \text{ and } S_e; \tag{19a}$$

$$\frac{\partial \phi_j}{\partial z} - \frac{\omega^2}{g} \phi_j = 0, \quad \text{on } S_i \text{ and } S_e; \tag{19b}$$

$$\frac{\partial \phi_R}{\partial z} - \frac{\omega^2}{g} \phi_R = \begin{cases} -1, & \text{on } S_i; \\ 0, & \text{on } S_e. \end{cases} \tag{19c}$$

On the body surface, the following conditions are held for the respective potentials:

$$\frac{\partial \phi_D}{\partial n} = -\frac{\partial \phi_I}{\partial n}, \quad \text{on } S_b; \tag{20a}$$

$$\frac{\partial \phi_j}{\partial n} = n_j, \quad \text{on } S_b; \tag{20b}$$

$$\frac{\partial \phi_R}{\partial n} = 0, \quad \text{on } S_b. \tag{20c}$$

A boundary integral equation method is then used. An oscillating source satisfying the free-surface boundary condition is employed as Green's function. The mathematical expression of the Green function is given as follows:

$$G(\mathbf{x},\ \mathbf{x}_0;\ \omega) = -\frac{1}{4\pi}\left(\frac{1}{r_1}+\frac{1}{r_2}\right)+\frac{1}{4\pi}\int_0^\infty \frac{2(\nu+\mu)\mathrm{e}^{-\mu h}\cosh\left[\mu(z+h)\right]\cosh\left[\mu(z_0+h)\right]}{\nu\cosh(\mu h)-\mu\sinh(\mu h)}J_0(\mu R)\,\mathrm{d}\mu, \tag{21}$$

in which

$$R = \sqrt{(x-x_0)^2+(y-y_0)^2}; \tag{22a}$$

$$r_1 = \sqrt{R^2+(z-z_0)^2}; \tag{22b}$$

$$r_2 = \sqrt{R^2+(z+z_0+2h)^2}. \tag{22c}$$

In the above equations, $J_0(\cdot)$ is the Bessel function of zeroth order; ν is equal to ω^2/g.

A Fredholm integral equation of the second kind for the potentials can be obtained after applying Green's second identity to the velocity potential and Green's function in the entire fluid domain. The resulting boundary-integral equations for ϕ_D, ϕ_j and ϕ_R are as follows:

$$\alpha\phi_D(\mathbf{x}_0)-\iint_{S_b}\frac{\partial G(\mathbf{x},\ \mathbf{x}_0;\ \omega)}{\partial n}\phi_D(\mathbf{x})\,\mathrm{d}s = \iint_{S_b} G(\mathbf{x},\ \mathbf{x}_0;\ \omega)\frac{\partial \phi_I}{\partial n}\,\mathrm{d}s; \tag{23a}$$

$$\alpha\phi_j(\mathbf{x}_0)-\iint_{S_b}\frac{\partial G(\mathbf{x},\ \mathbf{x}_0;\ \omega)}{\partial n}\phi_j(\mathbf{x})\,\mathrm{d}s = -\iint_{S_b} G(\mathbf{x},\ \mathbf{x}_0;\ \omega)n_j\,\mathrm{d}s, \quad (j=1,\ 2,\ ...,\ 6); \tag{23b}$$

$$\alpha\phi_R(\mathbf{x}_0)-\iint_{S_b}\frac{\partial G(\mathbf{x},\ \mathbf{x}_0;\ \omega)}{\partial n}\phi_R(\mathbf{x})\,\mathrm{d}s = \iint_{S_i} G(\mathbf{x},\ \mathbf{x}_0;\ \omega)\,\mathrm{d}s, \tag{23c}$$

in which α is a measurement of the normalised solid angle. When $\mathbf{x}_0$ is on S_i, α is equal to unity. When $\mathbf{x}_0$ is on S_b, α is evaluated by formulating a complementary problem within the interior of S_b. Alternative integral equations can be developed as below (e.g., for the pressure-dependent radiation problem):

$$\phi_R(\mathbf{x}_0)+\iint_{S_b}\left[\frac{\partial G_b(\mathbf{x},\ \mathbf{x}_0)}{\partial n}\phi_R(\mathbf{x}_0)-\frac{\partial G(\mathbf{x},\ \mathbf{x}_0;\ \omega)}{\partial n}\phi_R(\mathbf{x})\right]\mathrm{d}s = \iint_{S_i} G(\mathbf{x},\ \mathbf{x}_0;\ \omega)\,\mathrm{d}s, \tag{24}$$

where the auxiliary Green function G_b corresponds to a rigid free-surface condition and a no-flow condition on the sea bed.

HOBEM (Teng and Eatock Taylor, 1995) is then used to solve the boundary-integral equations. S_b and S_i are discretised into a number of 6-node quadratic triangular elements or 8-node quadratic quadrilateral elements for modelling both the geometry and the variation of potentials. Based on the idea of isoparametric transformation, the elements are transferred into those under isoparametric coordinates. The potential at an arbitrary point within an element is defined by its nodal values and shape function, and the integral within each element is evaluated using the Gauss-Legendre quadrature rule. Then, the collocation method is applied by locating the source point $\mathbf{x}_0$ on each node point to form a set of algebraic equations. After solving the linear algebraic system, the potentials over the body surface and the internal free surface are obtained.

4. Calculation of the motion response and wave power absorption

With the boundary value problem being solved, we turn to calculate the quantities of interest. The air volume flux can be determined according to

$$\hat{q} = \iint_{S_i} \frac{\partial\left(\phi_I + \phi_D\right)}{\partial z} \mathrm{d}s; \tag{25a}$$

$$q_j = \iint_{S_i} \left(\frac{\partial \phi_j}{\partial z} - e_j \right) \mathrm{d}s, \quad (j = 1,\ 2,\ \ldots,\ 6); \tag{25b}$$

$$q_R = \iint_{S_i} \frac{\partial \phi_R}{\partial z} \mathrm{d}s, \tag{25c}$$

where

$$e_j = \begin{cases} 1, & j = 3, \\ y - y_o, & j = 4, \\ -\left(x - x_o\right) & j = 5, \\ 0, & j = 1,\ 2,\ 6. \end{cases} \tag{26}$$

The force component $f_{w,j}$, which is due to the hydrodynamic pressure, is expressed in the form of

$$f_{w,j} = f_{e,j} + \sum_{l=1}^{6}\left[\left(\omega^2 a_{jl} + \mathrm{i}\omega b_{jl}\right)\xi_l\right] + f_{R,j}, \quad (j = 1,\ 2,\ ...,\ 6), \tag{27}$$

where $f_{e,j}$ is the wave exciting force component, and given by

$$f_{e,j} = \mathrm{i}\omega\rho\iint_{S_b}\left[\left(\phi_I + \phi_D\right)n_j\right]\mathrm{d}s, \quad (j = 1,\ 2,\ ...,\ 6); \tag{28}$$

a_{jl} and b_{jl} are the added mass and radiation damping, respectively, which are determined according to

$$\omega^2 a_{jl} + \mathrm{i}\omega b_{jl} = \omega^2\rho\iint_{S_b}\phi_l n_j \mathrm{d}s, \quad (j,\ l = 1,\ 2,\ ...,\ 6); \tag{29}$$

$f_{R,j}$ is contributed by the pressure-dependent radiation potential and defined by

$$f_{R,j} = \frac{p_c}{\rho g}L_{R,j}, \quad (j = 1,\ 2,\ ...,\ 6), \tag{30}$$

where the transfer function $L_{R,j}$ is expressed as

$$L_{R,j} = \omega^2\rho\iint_{S_b}\phi_R n_j \mathrm{d}s. \tag{31}$$

Besides the wave action, the oscillating air pressure within the chamber can also the cause dynamic force on the device. The dynamic air force can be determined through pressure integration over the instantaneous contact surface S_P. When the body motion is insignificant, the integral over S_P can be calculated using the quantities over the mean contact surface S_p through Taylor series expansions. We assume that the cross-sectional area of the air duct is small compared with the area of the internal free surface. Then, the dynamic air force $\mathbf{f}_c$ can be expressed as

$$f_{c,j} = \frac{p_c}{\rho g}L_{c,j}, \quad (j = 1,\ 2,\ ...,\ 6) \tag{32}$$

where the transfer function $L_{c,j}$ is defined by

$$\left\{L_{c,1},\ L_{c,2},\ L_{c,3}\right\}^T = \iint_{S_p}\rho g\mathbf{n}\mathrm{d}s = \rho g A_{wp}\mathbf{k}; \tag{33a}$$

$$\left\{L_{c,4},\ L_{c,5},\ L_{c,6}\right\}^T = \iint_{S_p}\rho g\left[\left(\mathbf{x} - \mathbf{x}_o\right)\times\mathbf{n}\right]\mathrm{d}s = \rho g A_{wp}\begin{Bmatrix} y_{c,f} - y_o \\ -\left(x_{c,f} - x_0\right) \\ 0 \end{Bmatrix}. \tag{33b}$$

In Eq. (33), A_{wp} is the area of the internal free surface S_i; $(x_{c,f}, y_{c,f})$ is the centre of S_i. The normal vector on S_p is defined as positive when pointing out the chamber.

The motion analysis of a rigid body is divided into two parts. In the first part, the total mass is concentrated at the centre of the gravity $\mathbf{x}_c$; in the other part, the angular rotation around the rotation centre $\mathbf{x}_o$ is considered. We further define

$$\xi_7 = \frac{p_c}{\rho g}. \tag{34}$$

Then, the equation of body motion in its six degrees of freedom can be written as

$$\sum_{l=1}^{6}\left\{\left[-\omega^2\left(m_{jl}+a_{jl}\right)-\mathrm{i}\omega\left(b_{jl}+B_{jl}\right)+\left(c_{jl}+K_{jl}\right)\right]\xi_l\right\}-\left(L_{R,j}+L_{c,j}\right)\xi_7 = f_{e,j}, \quad (j=1,\ 2,\ \ldots,\ 6), \tag{35}$$

where m_{jl} and c_{jl} are the components in the mass matrix and hydrostatic restoring matrix, respectively; B_{jl} is the linear structural damping coefficient; K_{jl} is the external linear stiffness coefficient. In addition, based on Eqs. (7) and (17), we can have

$$-\mathrm{i}\omega\sum_{j=1}^{6}\left(\xi_j q_j\right)-\left[\left(\chi-\mathrm{i}\omega\mu\right)\rho g+\mathrm{i}\omega q_R\right]\xi_7 = -\hat{q}. \tag{36}$$

After combining Eqs. (35) and (36), seven linear equations with an equal number of unknowns can be established. After solving the linear algebraic system and obtaining the body motions and the oscillating air pressure, the free-surface elevation amplitude can be calculated using the kinematic condition on the free surface. That is

$$\eta = -\frac{1}{\mathrm{i}\omega}\frac{\partial\phi}{\partial z}\bigg|_{z=0} = -\frac{1}{\mathrm{i}\omega}\left[\frac{\partial\phi_I}{\partial z}+\frac{\partial\phi_D}{\partial z}-\mathrm{i}\omega\sum_{j=1}^{6}\left(\xi_j\frac{\partial\phi_j}{\partial z}\right)-\mathrm{i}\omega\frac{p_c}{\rho g}\frac{\partial\phi_R}{\partial z}\right]\bigg|_{z=0}. \tag{37}$$

5. Optimal turbine parameter for floating OWCs

The optimal turbine parameter, with which the device has the maximum wave power absorption, is discussed in this section. A decomposition of the body motion response is therefore made by

$$\xi_j = u_j + \xi_7 v_j, \quad (j=1,\ 2,\ \ldots,\ 7), \tag{38}$$

where u_j is the motion response of the device without the effect of the oscillating air pressure (i.e., the top of the chamber being entirely open to the atmosphere); v_j is that due to the oscillating air pressure in the absence of incident waves. In other words, u_j is purely induced by the wave exciting force, while v_j is induced by the pressure-dependent radiation force together with the dynamic air force. Then, u_j and v_j can be obtained by solving the following equations

$$\sum_{l=1}^{6}\left\{\left[-\omega^2\left(m_{jl}+a_{jl}\right)-\mathrm{i}\omega\left(b_{jl}+B_{jl}\right)+\left(c_{jl}+K_{jl}\right)\right]u_l\right\}=f_{e,j},\quad (j=1,\ 2,\ ...,\ 6) \tag{39a}$$

$$u_7=0, \tag{39b}$$

and

$$\sum_{l=1}^{6}\left\{\left[-\omega^2\left(m_{jl}+a_{jl}\right)-\mathrm{i}\omega\left(b_{jl}+B_{jl}\right)+\left(c_{jl}+K_{jl}\right)\right]v_l\right\}=L_{R,j}+L_{c,j},\quad (j=1,\ 2,\ ...,\ 6) \tag{40a}$$

$$v_7=1. \tag{40b}$$

Eqs. (39) and (40) indicate that the solutions of u_j and v_j are both independent of the chamber and turbine parameters.

By using Eqs. (36) and (38), we can obtain

$$p_c=-\frac{\hat{q}-\mathrm{i}\omega\sum_{j=1}^{6}\left(u_jq_j\right)}{-\frac{\mathrm{i}\omega}{\rho g}\sum_{j=1}^{6}\left(v_jq_j\right)-\frac{\mathrm{i}\omega}{\rho g}q_R-\left(\chi-\mathrm{i}\omega\mu\right)}. \tag{41}$$

In the meantime, after substituting Eq. (38) into Eq. (17), the air volume flux can be decomposed into the following form:

$$q_c=q_w-p_c\left(C_b-\mathrm{i}C_a\right), \tag{42}$$

where

$$q_w=\hat{q}-\mathrm{i}\omega\sum_{j=1}^{6}\left(u_jq_j\right); \tag{43a}$$

$$-\left(C_b-\mathrm{i}C_a\right)=-\sum_{j=1}^{7}\left[v_j\left(C_{b,j}-\mathrm{i}C_{a,j}\right)\right], \tag{43b}$$

with

$$-\frac{\mathrm{i}\omega}{\rho g}q_j=-\left(C_{b,j}-\mathrm{i}C_{a,j}\right),\quad (j=1,\ 2,\ \ldots,\ 6); \tag{44a}$$

$$-\frac{\mathrm{i}\omega}{\rho g}q_R=-\left(C_{b,7}-\mathrm{i}C_{a,7}\right). \tag{44b}$$

In Eq. (43), q_w is the air volume flux of a free-floating or moored device when there is no oscillating air pressure. The application of Green's second identify to ϕ_R and ϕ_D (or ϕ_j) in the entire fluid domain can lead to

$$\iint_{S_i}\frac{\partial\phi_D}{\partial z}\mathrm{d}s=\frac{\omega^2}{g}\iint_{S_b}\phi_R\frac{\partial\phi_I}{\partial n}\mathrm{d}s; \tag{45a}$$

$$\iint_{S_i}\frac{\partial\phi_j}{\partial z}\mathrm{d}s=-\frac{\omega^2}{g}\iint_{S_b}\phi_R n_j\mathrm{d}s. \tag{45b}$$

Then, by using Eqs. (25) and (43a), we can have

$$q_w=\frac{\omega^2}{g}\left\{\iint_{S_b}\left[\phi_R\frac{\partial\phi_I}{\partial n}-\mathrm{i}\omega\sum_{j=1}^{6}\left(-u_j\phi_R n_j\right)\right]\mathrm{d}s+\iint_{S_i}\phi_I\mathrm{d}s\right\}. \tag{46}$$

Eq. (46) provides an alternative way to calculate q_w.

Analogous to the definition in electric circuit theory (Falnes and Mciver, 1985), here $C_b-\mathrm{i}C_a$ is defined as the radiation admittance for moving OWCs with C_a the radiation susceptance and C_b the radiation conductance. Referring to Falnes (2002), the captured wave power becomes

$$W_c=\frac{1}{2}\chi\frac{\left|\hat{q}-\mathrm{i}\omega\sum_{j=1}^{6}\left(u_j q_j\right)\right|^2}{\left[\chi+\sum_{j=1}^{7}\left(v_j C_{b,j}\right)\right]^2+\left[\omega\mu+\sum_{j=1}^{7}\left(v_j C_{a,j}\right)\right]^2}. \tag{47}$$

To maximise the energy extraction efficiency, the optimal turbine parameter χ_{opt} is then solved. As the chamber's size and geometry cannot be easily adjusted, μ cannot be optimised for a broad range of wave conditions. Hence, only the power take-off system

is adjusted (i.e., the parameter χ) to get the maximum efficiency for the given dimensions of an air chamber. Then, Eq. (47) is differentiated with respect to χ to obtain the following condition for a maximum wave power absorption

$$\chi_{opt} = \sqrt{\left[\sum_{j=1}^{7}\left(v_j C_{b,j}\right)\right]^2 + \left[\omega\mu + \sum_{j=1}^{7}\left(v_j C_{a,j}\right)\right]^2}. \tag{48}$$

The use of Eqs. (47) and (48) gives

$$W_{c,\,\max} = \frac{1}{2}\frac{\sqrt{\left[\sum_{j=1}^{7}\left(v_j C_{b,j}\right)\right]^2 + \left[\omega\mu + \sum_{j=1}^{7}\left(v_j C_{a,j}\right)\right]^2}\cdot\left|\hat{q} - \mathrm{i}\omega\sum_{j=1}^{7}\left(u_j q_j\right)\right|^2}{\left\{\sqrt{\left[\sum_{j=1}^{7}\left(v_j C_{b,j}\right)\right]^2 + \left[\omega\mu + \sum_{j=1}^{7}\left(v_j C_{a,j}\right)\right]^2} + \sum_{j=1}^{7}\left(v_j C_{b,j}\right)\right\}^2 + \left[\omega\mu + \sum_{j=1}^{7}\left(v_j C_{a,j}\right)\right]^2}. \tag{49}$$

When the device is stationary in waves, we can have

$$u_j = v_j = 0,\ \left(j = 1,\ 2,\ \ldots,\ 6\right) \tag{50a}$$

and

$$-\left(C_b - \mathrm{i}C_a\right) = -\left(C_{b,\,7} - \mathrm{i}C_{a,\,7}\right). \tag{50b}$$

Then, Eqs. (48) and (49) are reduced to

$$\chi_{opt} = \sqrt{\left(C_{b,\,7}\right)^2 + \left(\omega\mu + C_{a,\,7}\right)^2}, \tag{51}$$

and

$$W_{c,\,\max} = \frac{1}{2}\frac{\sqrt{C_{b,\,7}^2 + \left(\omega\mu + C_{a,\,7}\right)^2}\cdot\left|\hat{q}\right|^2}{\left[\sqrt{C_{b,\,7}^2 + \left(\omega\mu + C_{a,\,7}\right)^2} + C_{b,\,7}\right]^2 + \left(\omega\mu + C_{a,\,7}\right)^2}, \tag{52}$$

which are essentially the same as the derivation in Martins-Rivas and Mei (2009) for stationary devices.

If the effect of air compressibility is neglected and the phase difference between the oscillating air pressure and air mass flux is assumed zero (i.e., $\mu = 0$), Eqs. (48) and (49) can be further reduced to

$$\chi_{opt} = \sqrt{C_{a,\,7}^2 + C_{b,\,7}^2}, \tag{53}$$

and

$$W_{c,\max} = \frac{1}{2} \frac{\sqrt{C_{a,7}^2 + C_{b,7}^2} \cdot |\hat{q}|^2}{\left(\sqrt{C_{a,7}^2 + C_{b,7}^2} + C_{b,7}\right)^2 + C_{a,7}^2}, \tag{54}$$

which are the same as the derivation in Evans and Porter (1997) for stationary devices and incompressible air.

6. Calculation of mean wave drift force on OWCs using momentum conservation

It is generally understood that the second-order difference-frequency wave force is the main excitation of the slow-drift motion. Reliable semi-analytical and numerical solutions for the second-order wave force in bi-chromatic waves have been developed by researchers such as Kim and Yue (1990), Eatock Taylor and Huang (1997), Teng and Cong (2017), Cong et al. (2012, 2018), Heo and Kashiwagi (2020) and Shao et al. (2022). When the frequency difference is small, Newman (1974) expanded the complete difference-frequency wave force into Taylor's series with respect to the frequency difference, and only the zero-order component is retained. As a consequence, the exact difference-frequency wave force is approximated by the mean wave drift force on structures in regular waves. Due to the importance of the mean wave drift force to the low-frequency behaviour of a floating body, numerical methods with high precision have been developed by researchers to calculate the mean wave drift force. Examples include Choi et al. (2001), Newman and Lee (2002), Kashiwagi et al. (2005) and Shao (2018).

For structures without an internal free surface subjected to the oscillating air pressure, different methods have been developed for the mean wave drift force or moment, such as those based on the direct pressure integration or applying momentum conservation. The former approach can be extended to the cases of OWC devices in a straightforward manner. This has been achieved in some previous studies, such as Hong et al. (2004) and Konispoliatis and Mavrakos (2016). The method based on the use of momentum conservation is normally considered more accurate (Ledoux et al., 2006), and hence it is adopted here for the OWC devices.

By using the kinematic transport theorem and Gauss theorem, the following

expression can be obtained for the linear momentums $\mathbb{M}_x$ and $\mathbb{M}_y$ (see Mei et al., 2005)

$$\frac{\mathrm{d}}{\mathrm{d}t}\begin{Bmatrix}\mathbb{M}_x\\ \mathbb{M}_y\end{Bmatrix}=-\iint_{S_B\cup S_\infty\cup S_d\cup S_F}\left[P\begin{Bmatrix}n_x\\ n_y\end{Bmatrix}+\rho\begin{Bmatrix}u\\ v\end{Bmatrix}\left(\mathbf{u}\cdot\mathbf{n}-U_n\right)\right]\mathrm{d}s. \tag{55}$$

in which S_∞ is a circular cylindrical surface enclosing the device, and its radius tends to infinity; $\mathbf{u} = (u, v, w)^T$ is the vector of the fluid velocity; U_n is the normal velocity of the boundary surface. On S_F and S_d, it is required that $\mathbf{u}\cdot\mathbf{n} - U_n = 0$. The control surface at infinity is fixed, yielding $U_n = 0$ on S_∞. Outside the chamber, the fluid pressure over the free surface is equivalent to atmospheric pressure that is assumed zero.

Then, we can relate the wave force on the system to the linear momentum in the fluid domain. That is

$$\begin{Bmatrix}F_x\\ F_y\end{Bmatrix}=\iint_{S_B}P\begin{Bmatrix}n_x\\ n_y\end{Bmatrix}\mathrm{d}s=-\iint_{S_\infty}\left[P\begin{Bmatrix}n_x\\ n_y\end{Bmatrix}+\rho\begin{Bmatrix}u\\ v\end{Bmatrix}\mathbf{u}\cdot\mathbf{n}\right]\mathrm{d}s-\iint_{S_I}P_c\begin{Bmatrix}n_x\\ n_y\end{Bmatrix}\mathrm{d}s-\frac{\mathrm{d}}{\mathrm{d}t}\begin{Bmatrix}\mathbb{M}_x\\ \mathbb{M}_y\end{Bmatrix}, \tag{56}$$

where S_I represents the instantaneous free surface inside the chamber. We consider the case when the oscillating air pressure over S_I is uniformly distributed. By using the Taylor series expansion, the integration over S_I can be further expressed as:

$$\iint_{S_I}P_c\begin{Bmatrix}n_x\\ n_y\end{Bmatrix}\mathrm{d}s=-\oint_{\Gamma_i}P_c\zeta\begin{Bmatrix}n_x\\ n_y\end{Bmatrix}\mathrm{d}l+O\left(\varepsilon^2\right). \tag{57}$$

where ε is the wave steepness; Γ_i is the intersection of the mean body surface with the undisturbed internal free surface S_i. Then, the second-order mean wave drift force on the device is expressed as

$$\begin{Bmatrix}f_x^-\\ f_y^-\end{Bmatrix}=\begin{Bmatrix}f_{f,x}^-\\ f_{f,y}^-\end{Bmatrix}+\begin{Bmatrix}f_{n,x}^-\\ f_{n,y}^-\end{Bmatrix}, \tag{58}$$

where

$$f_{f,x}^-=\overline{\rho\iint_{S'_\infty}\left[\frac{1}{2}\left(\nabla\Phi^{(1)}\cdot\nabla\Phi^{(1)}\right)n_x-\frac{\partial\Phi^{(1)}}{\partial x}\frac{\partial\Phi^{(1)}}{\partial r}\right]\mathrm{d}s}-\overline{\frac{1}{2}\rho g\oint_{\Gamma'_\infty}\left(\zeta^{(1)}\right)^2n_x\mathrm{d}l}; \tag{59a}$$

$$f_{f,y}^-=\overline{\rho\iint_{S'_\infty}\left[\frac{1}{2}\left(\nabla\Phi^{(1)}\cdot\nabla\Phi^{(1)}\right)n_y-\frac{\partial\Phi^{(1)}}{\partial y}\frac{\partial\Phi^{(1)}}{\partial r}\right]\mathrm{d}s}-\overline{\frac{1}{2}\rho g\oint_{\Gamma'_\infty}\left(\zeta^{(1)}\right)^2n_y\mathrm{d}l}, \tag{59b}$$

and

$$\begin{Bmatrix} f_{n,x}^{-} \\ f_{n,y}^{-} \end{Bmatrix} = \overline{\oint_{\Gamma_i} P_c \zeta \begin{Bmatrix} n_x \\ n_y \end{Bmatrix} \mathrm{d}l} = \overline{-\frac{P_c}{\rho g} \oint_{\Gamma_i} \left(\rho \frac{\partial \Phi}{\partial t} + P_c \right) \begin{Bmatrix} n_x \\ n_y \end{Bmatrix} \mathrm{d}l}. \tag{60}$$

In Eq. (59), S'_∞ is the control surface in calm water, extending from seabed to $z = 0$; Γ'_∞ is the intersection of S'_∞ with $z = 0$; $f_{f,x}^{-}$ and $f_{f,y}^{-}$ are the terms contributed by far-field quantities; $f_{n,x}^{-}$ and $f_{n,y}^{-}$ are owing to the oscillating air pressure within the chamber. As the internal free surface is not connected to the exterior region, Eq. (60) can be reduced to

$$\begin{Bmatrix} f_{n,x}^{-} \\ f_{n,y}^{-} \end{Bmatrix} = \overline{-\frac{P_c}{\rho g} \oint_{\Gamma_i} \left(\rho \frac{\partial \Phi}{\partial t} \right) \begin{Bmatrix} n_x \\ n_y \end{Bmatrix} \mathrm{d}l}. \tag{61}$$

For regular incident waves, $f_{f,x(y)}^{-}$ and $f_{n,x(y)}^{-}$ can be expressed as

$$f_{f,x}^{-} = \mathrm{Re}\left\{ \frac{\rho}{4} \iint_{S'_\infty} \left[\left(\nabla\phi \cdot \nabla\phi^* \right) \cos\theta - 2 \frac{\partial \phi}{\partial x} \frac{\partial \phi^*}{\partial r} \right] \mathrm{d}s - \frac{\rho}{4} \frac{\omega^2}{g} \oint_{\Gamma'_\infty} \left(\phi\phi^* \cos\theta \right) \mathrm{d}l \right\}; \tag{62a}$$

$$f_{f,y}^{-} = \mathrm{Re}\left\{ \frac{\rho}{4} \iint_{S'_\infty} \left[\left(\nabla\phi \cdot \nabla\phi^* \right) \sin\theta - 2 \frac{\partial \phi}{\partial y} \frac{\partial \phi^*}{\partial r} \right] \mathrm{d}s - \frac{\rho}{4} \frac{\omega^2}{g} \oint_{\Gamma'_\infty} \left(\phi\phi^* \sin\theta \right) \mathrm{d}l \right\}. \tag{62b}$$

and

$$\begin{Bmatrix} f_{n,x}^{-} \\ f_{n,y}^{-} \end{Bmatrix} = -\mathrm{Re}\left\{ \frac{\mathrm{i}\omega}{2g} p_c \oint_{\Gamma_i} \phi^* \begin{Bmatrix} n_x \\ n_y \end{Bmatrix} \mathrm{d}l \right\}. \tag{63}$$

Following a similar manner as the derivation for the wave force, the mean wave drift moment around the vertical axis of the device can also be expressed as a summation of the two distinct terms. Then, we can have

$$m_z^{-} = m_{f,z}^{-} + m_{n,z}^{-}, \tag{64}$$

where

$$m_{f,z}^{-} = \overline{-\rho \iint_{S'_\infty} \frac{\partial \Phi}{\partial \theta} \frac{\partial \Phi}{\partial r} \mathrm{d}s}; \tag{65a}$$

$$m_{n,z}^{-} = \overline{\mathbf{k} \cdot \left\{ -\frac{P_c}{\rho g} \oint_{\Gamma_i} \left(\rho \frac{\partial \Phi}{\partial t} \right) \left[\left(\mathbf{x} - \mathbf{x}_o \right) \times \mathbf{n} \right] \mathrm{d}s \right\}}. \tag{65b}$$

For regular incident waves, $m_{f,z}^{-}$ and $m_{n,z}^{-}$ can be expressed as

$$\bar{m}_{f,z} = \mathrm{Re}\left[-\frac{\rho}{2} \iint_{S'_\infty} \frac{\partial \phi}{\partial \theta} \frac{\partial \phi^*}{\partial r} \mathrm{d}s \right], \tag{66}$$

and

$$\bar{m}_{n,z} = -\mathrm{Re}\left\{ \frac{\mathrm{i}\omega}{2g} \rho_c \oint_{\Gamma_i} \phi^* \left\{ \mathbf{k} \cdot \left[(\mathbf{x} - \mathbf{x}_o) \times \mathbf{n} \right] \right\} \mathrm{d}s \right\}. \tag{67}$$

7. Numerical results and discussion

Calculations are then conducted using the established model. In subsequent calculations, we use $\rho = 1.023\times10^3$ kg/m^3, $\rho_a = 1.293$ kg/m^3, $g = 9.807$ m/s^2, and $c = 340$ m/s. When in calm water, the air volume inside the chamber is expressed as

$$V_0 = h_0 A_{wp}, \tag{68}$$

where h_0 is the equivalent height of the entrapped air in calm water.

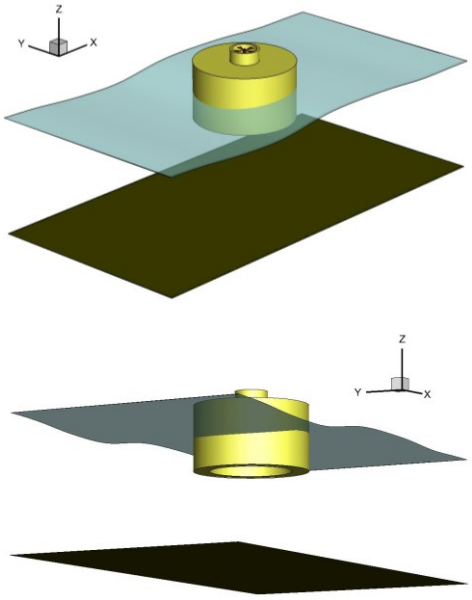

Fig. 2 Sketch of a floating cylindrical OWC device

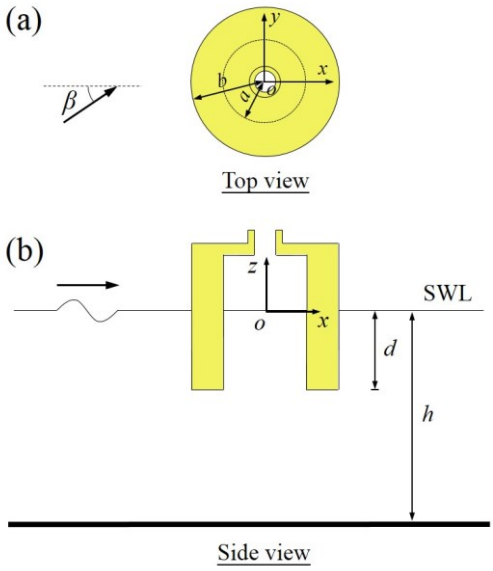

Fig. 3 Definition of the coordinate system for a floating cylindrical OWC device

7.1 Convergence test and validation

The convergence and validity of the developed model are examined in this section. A floating cylindrical OWC (see Fig. 2) is concerned in the examination. As shown in Fig. 3, the submerged part of the device is a cylindrical hollow column with its inner and outer radius being a and b, respectively. The draft of the device is d. In the

calculations, the Cartesian coordinate system is built with its origin at the centre of the undisturbed internal free surfer.

The convergence of the results with respect to the mesh discretisation is examined. Two different drafts, i.e., d = 2.5 m and 3.0 m, are concerned in the examination. Two discretised meshes, referred to as Mesh 1 and Mesh 2, are used for each draft. When d = 2.5 m, each quadrant is discretised with 136 and 252 quadrilaterals elements in Mesh 1 and Mesh 2, respectively. While, for d = 3 m, 152 and 300 elements are used in each quadrant, respectively. The meshes for d = 3 m have been given in Fig. 4 as an example. Computations are then conducted for the optimal turbine parameter and the mean wave drift force. As shown in Figs. 5 and 6, the results based on different meshes are in good agreement.

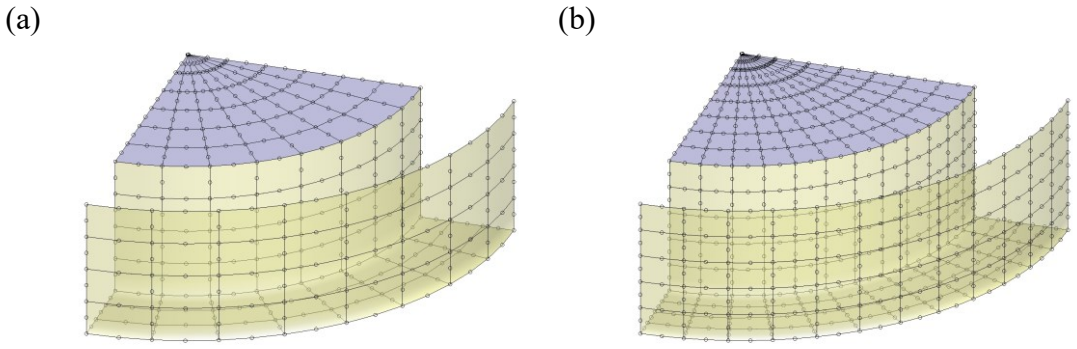

Fig. 4 Mesh discretisation in a quarter area for a computational case with a = 5 m, b = 7 m, and d = 3 m with different discretisation schemes: (a) Mesh 1, and (b) Mesh 2

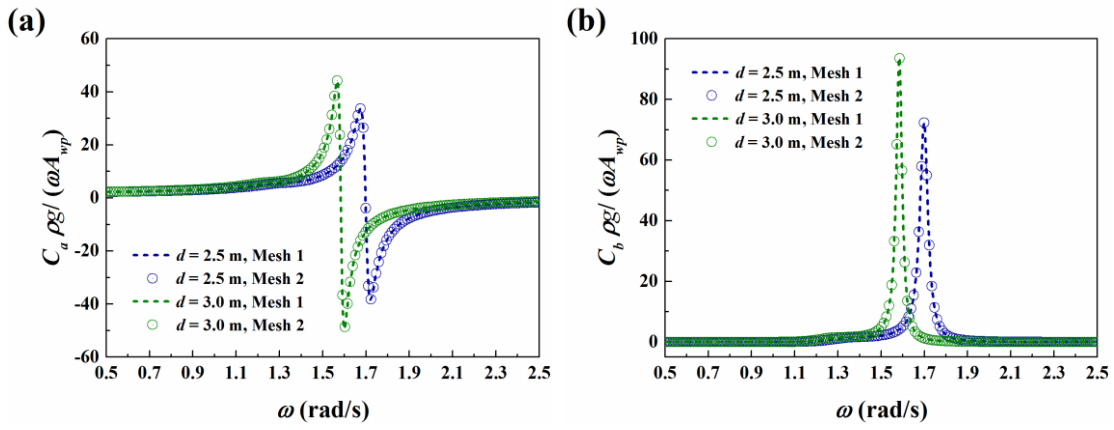

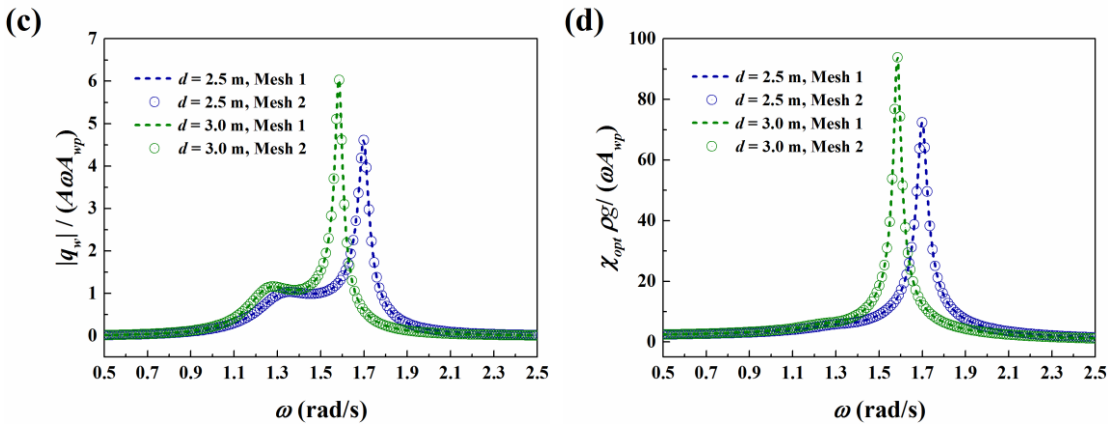

Fig. 5 Comparison of the optimal turbine parameter based on different computational meshes for free-floating cylindrical OWCs with a = 5 m, b = 7 m, and h = 20 m for: (a) C_a, (b) C_b, (c) q_w, and (d) χ_{opt}

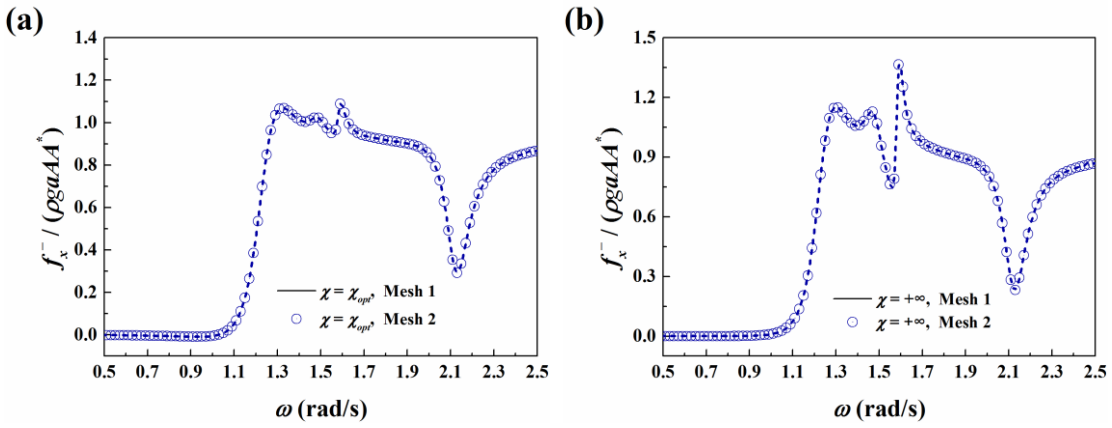

Fig. 6 Comparison of the mean wave drift force based on different computational meshes for free-floating cylindrical OWCs with a = 5 m, b = 7 m, d = 3.0 m, h_0 = 2.5 m, D = 1 m, K = 0.45, and h = 20 m for: (a) $\chi = \chi_{opt}$, and (b) $\chi = +\infty$.

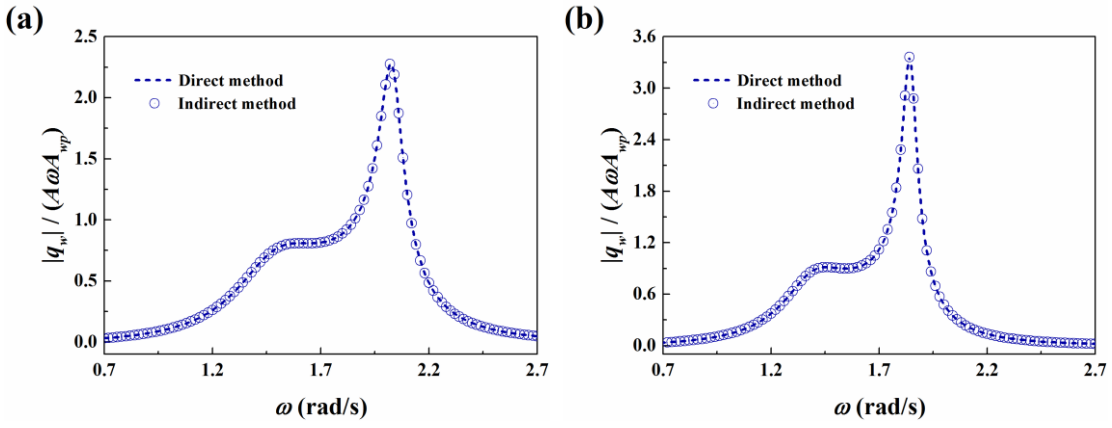

Fig. 7 Comparison of q_w based on different methods for free-floating cylindrical OWCs with a = 5 m, b = 7 m, d = 3.0 m, and h = 20 m with (a) d = 1.5 m, and (b) d = 2.0 m.

In this study, two different ways have been developed to evaluate q_w. One is based

519 on the integration of vertical fluid velocity over the interval free surface (see Eqs. (25)
520 and (43)). In the other one, q_w is evaluated with the aid of ϕ_R, and the solutions of ϕ_D
521 and ϕ_j are not involved (see Eq. (46)). The two methods are referred to as the 'direct'
522 and 'indirect' methods. For the purpose of validation, the results of q_w based on the
523 two methods are compared with each other, and a good agreement can be observed from
524 the comparison shown in Fig. 7.

525 The developed numerical model is also applicable for stationary devices. The cases
526 of stationary OWCs have been considered in earlier works, such as Evans and Porter
527 (1997), Martins-Rivas and Mei (2009), and Deng et al. (2013). The validity of the
528 developed model is then examined through a comparison with the published results.
529 Stationary cylindrical OWCs with thin shells are then concerned. The water depth is
530 fixed at $h = 2a$, and the draft of the device varies as $d = 0.4a$ and a, respectively. When
531 HOBEM is used, the thickness of the device is set as $0.01a$, i.e., $b - a = 0.01a$. A self-
532 adaptive Gauss integration method has been used to treat the nearly singular integration
533 that may occur for structures with thin elements. Figs. 8 and 9 show that the present
534 results agree well with the published data.

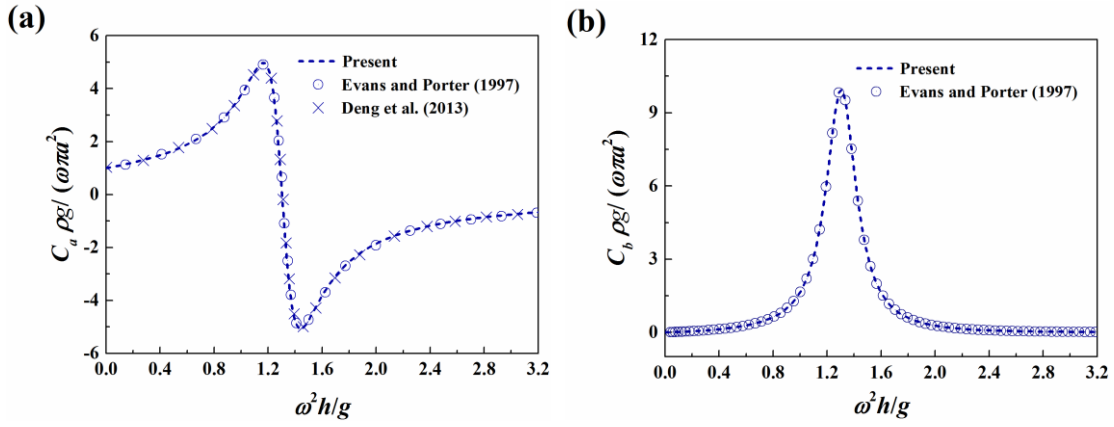

535

536 Fig. 8 Comparison of the present results with reported data for stationary OWC devices with $h = 2a$,
537 and $d = a$: (a) C_a, and (b) C_b

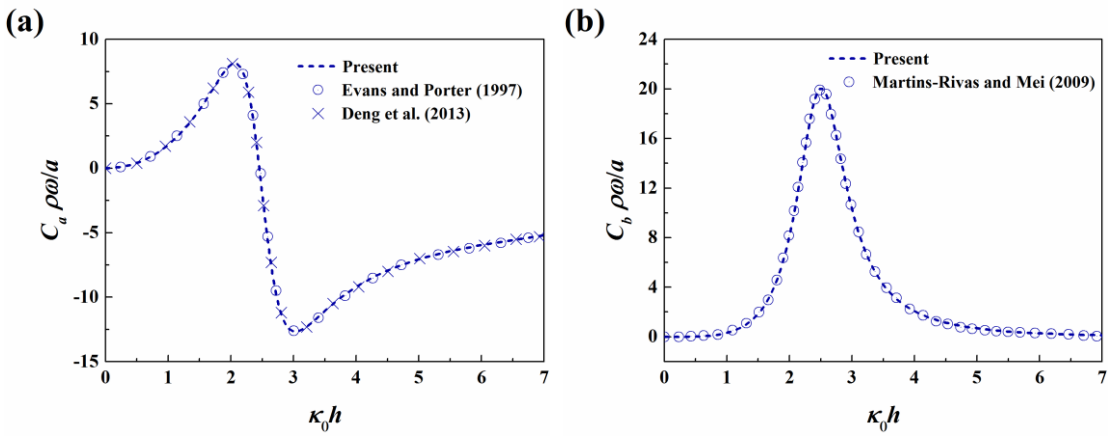

Fig. 9 Comparison of the present results with reported data for stationary OWC devices with $h = 2a$, and $d = 0.4a$: (a) C_a, and (b) C_b

After examining the convergence and validity of the developed model, detailed numerical studies are conducted. In subsequent calculations, the interior and exterior radius of the cylindrical chamber are set as $a = 5$ m and $b = 7$ m, respectively. The water depth is $h = 20$ m, and the height of the entrapped air in calm water is $h_0 = 2.5$ m. In addition, the diameter of the turbine rotor D is 1.0 m, and the empirical coefficient K is 0.45. The optimal turbine parameter χ_{opt} is used in the calculation unless stated elsewhere. Firstly, computations are conducted for free-floating cylindrical OWCs. Then, the optimisation of the geometry is made, and the cases that cylindrical OWCs with an attached arc-shaped reflector or connected to a submerged caisson are concerned.

7.2 Free-floating cylindrical OWC devices

Free-floating cylindrical OWCs are firstly concerned. In the calculation, incident waves travel along the positive x-axis. We assume that the submerged part accounts for the total mass of the device that is uniformly distributed. The mass matrix of the system is calculated accordingly. The detailed expression of m_{jl} and c_{jl} is given in the Appendix. In addition, external damping and stiffness are not considered in this section.

7.2.1 Surge, heave and pitch motions of free-floating cylindrical OWCs

In Figs. 10 and 11, the normalised added mass and radiation damping for surge and pitch are plotted against wave frequency. The results for different drafts exhibit similar behaviour. Taking d = 1.5m as an example, the depicted results show peculiar behaviour in the neighbourhood of ω = 2.06 rad/s. At this frequency, the wavelength is close to that of free fluid motion in a cylindrical container with a bottom. The fluid experiences a resonant motion of an anti-symmetric mode, namely sloshing. As the draft increases, the resonance region moves to the lower-frequency side with a narrower bandwidth. It is noted that there is a sudden sign change (from positive to negative) of the added mass a_{11} and a_{55} in close proximity to the resonance frequency of sloshing motion. Analogous phenomena for cylindrical moonpools have been reported in previous studies, such as Mavrakos (1985) and Yeung and Wang (2018).

The distribution of free-surface elevation amplitude in the vicinity of the device is shown in Figs. 12 and 13 at the resonance frequency of sloshing motion. The free-surface elevation within the chamber is anti-symmetric with respect to the y-axis. The sloshing phenomenon within a free-floating OWC is far less evident than in a stationary one, mainly due to the disturbance of radiation waves.

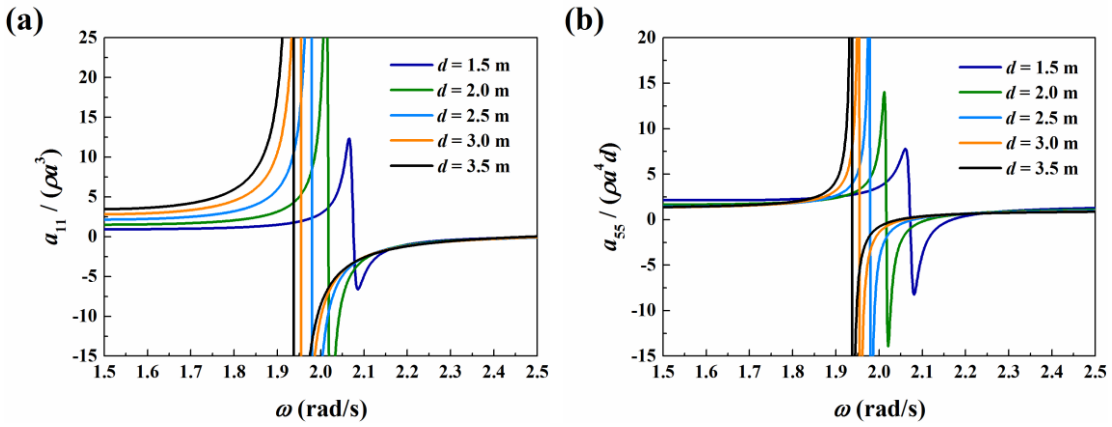

Fig. 10 Variation of the added mass of cylindrical OWCs for surge and pitch motions with a = 5 m, and b = 7 m: (a) a_{11}, and (b) a_{55}

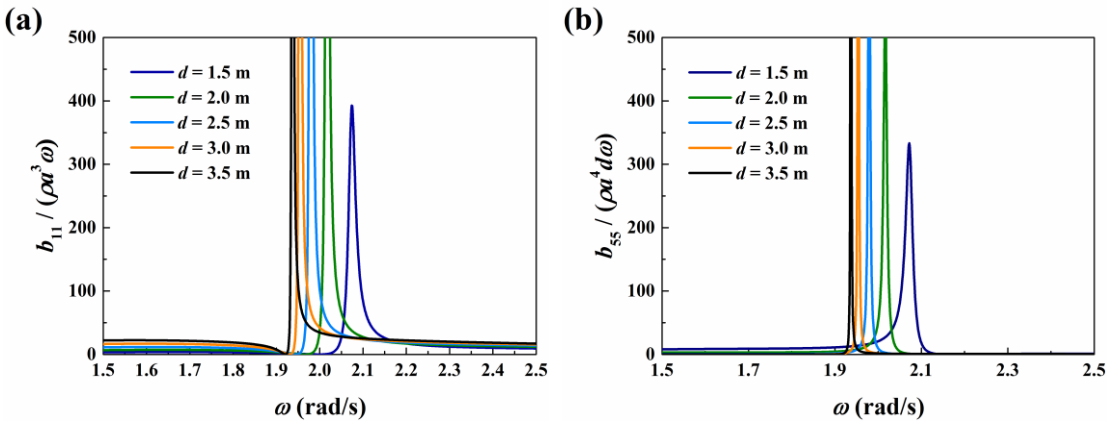

Fig. 11 Variation of the radiation damping of cylindrical OWCs for surge and pitch motions with a = 5 m, and b = 7 m: (a) b_{11}, and (b) b_{55}

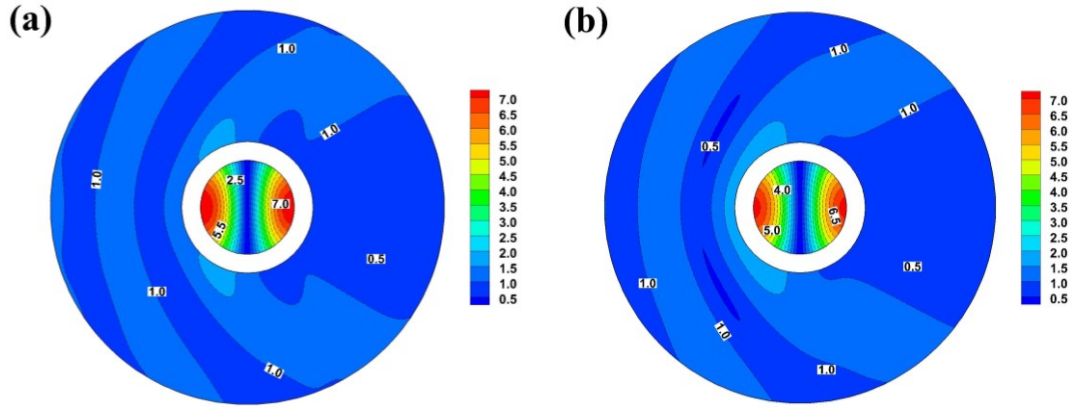

Fig. 12 Free-surface elevation amplitude around stationary OWCs with a = 5 m, b = 7 m, and χ = χ_{opt}: (a) d = 2.0 m, ω = 2.01 rad/s, and (b) d = 3 m, ω = 1.95 rad/s.

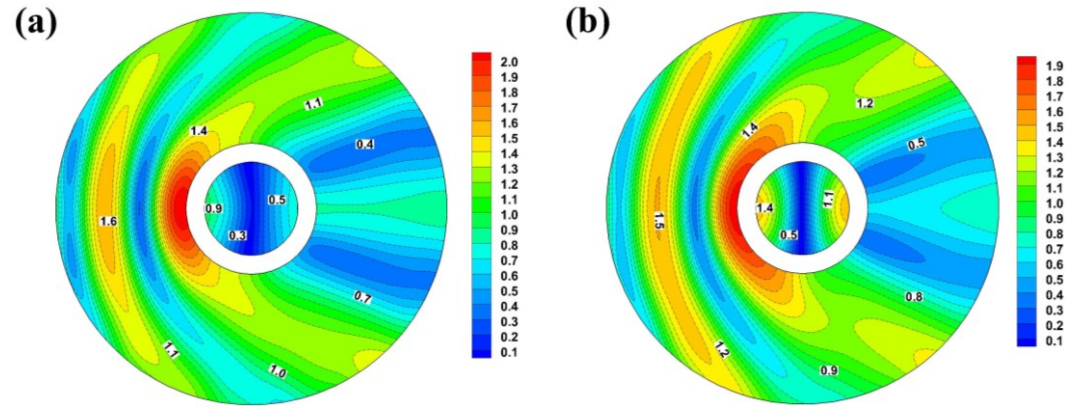

Fig. 13 Free-surface elevation amplitude around free-floating OWCs with a = 5 m, b = 7 m, and χ = χ_{opt}: (a) d = 2.0 m, ω = 2.01 rad/s, and (b) d = 3 m, ω = 1.95 rad/s.

As shown in Fig. 14, the wave excitation force for surge or pitch motion exhibits similar behaviour to the radiation damping. Owing to the coupling effects between the anti-symmetric motion modes, the prominent peaks of surge and pitch motions coincide

(see Fig. 15). Due to the lack of restoring force, the surge motion is remarkable in the low-frequency region. In addition, unlike the exciting force, surge and pitch motions are not significantly amplified around the resonance frequency of sloshing motion, probably attributed to the largely enhanced radiation damping around this frequency. It should also be noted that due to the device's symmetry, the anti-symmetric motion modes, i.e., surge and pitch, cannot generate air volume flux within the chamber and hence do not contribute to wave power absorption.

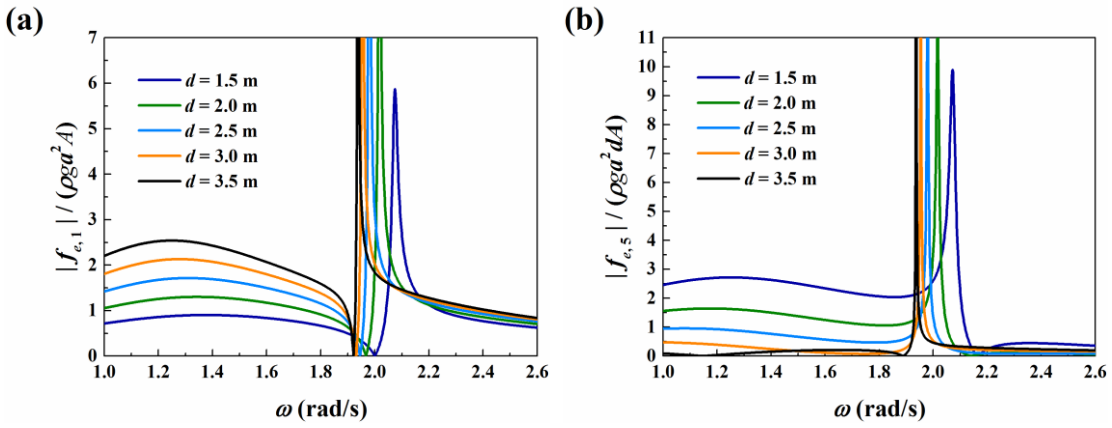

Fig. 14 Variation of the wave exciting force on cylindrical OWCs for surge and pitch motions with a = 5 m, and b = 7 m: (a) $f_{e,1}$, and (b) $f_{e,5}$

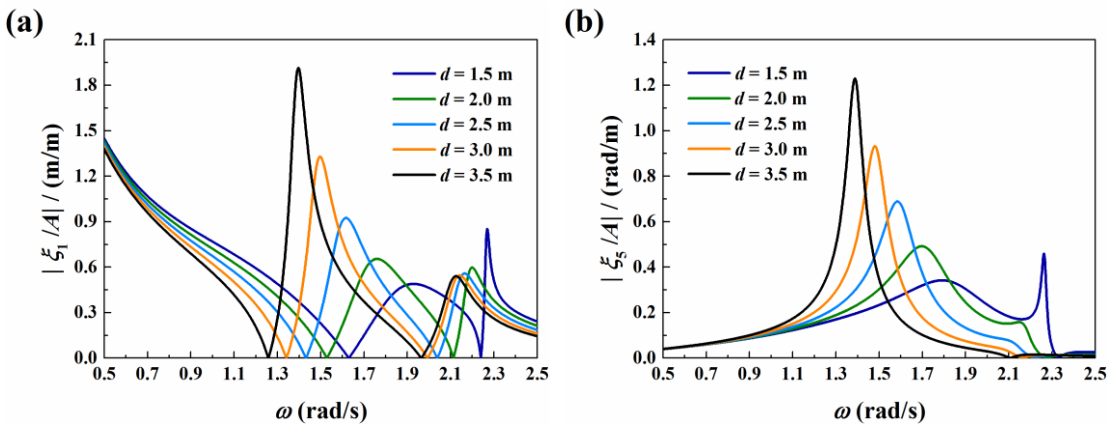

Fig. 15 Variation of the motion amplitude of cylindrical OWCs with a = 5 m, b = 7 m, and $\chi = \chi_{opt}$ for different drafts: (a) surge, and (b) pitch

The heave motion of free-floating cylindrical OWCs is then discussed. Fig. 16 depicts the added mass and radiation damping for heave motion against different drafts. Negative added mass is presented over a range of wave frequencies. Similar phenomena are also noticed in some studies for a body submerged underneath the free surface or

having an interior free surface. It was explained in terms of the resonant standing waves above or within the body (Mciver and Evans, 1984). In Fig. 16(a), over the negative added mass frequency range, the wavelengths are close to those of the free fluid motion in a cylindrical container with a bottom, and the fluid within experiences the resonant motion of a symmetric mode, namely piston. Due to the influence of the resonant piston motion, the added mass in Fig. 16(a) becomes negative over a specific frequency range. We also note that the negative added mass is accompanied by the rapid variation of radiation damping with frequency (see Fig. 16(b)).

Figs. 17 and 18 show the free-surface elevation amplitude at the resonance frequency of piston motion around a stationary and a free-floating OWC, respectively. The results indicate that the radiation waves can cause an apparent breakdown of the piston-mode fluid motion within the chamber.

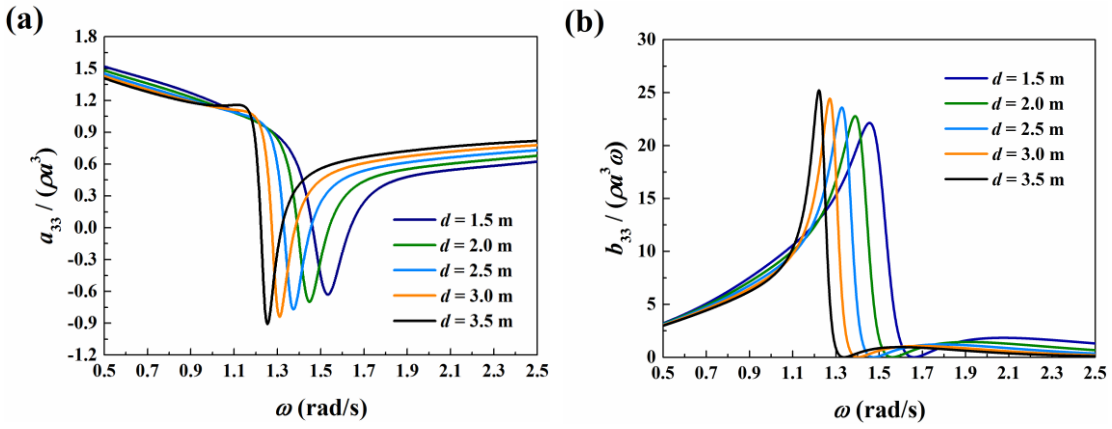

Fig. 16 Variation of the added mass and radiation damping of cylindrical OWCs for heave motion with a = 5 m, and b = 7 m: (a) a_{33}, and (b) b_{33}

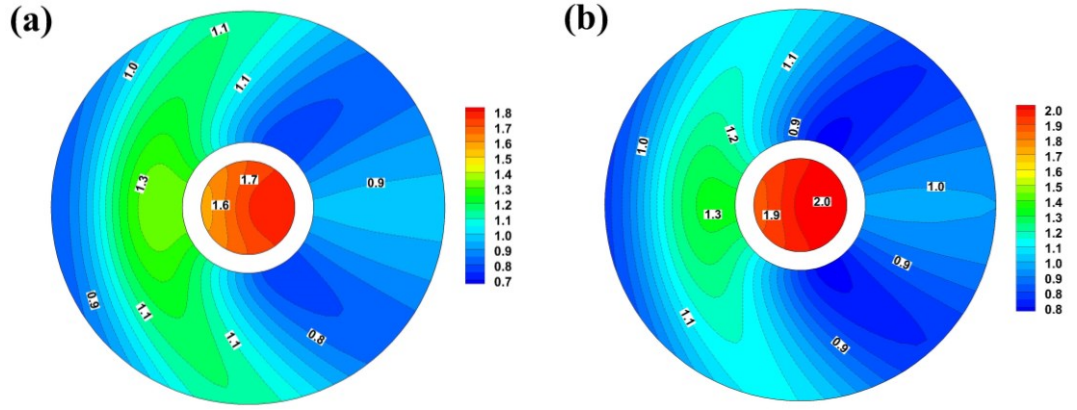

Fig. 17 Distribution of the free-surface elevation amplitude around stationary OWCs with a = 5 m, b = 7 m, and $\chi = \chi_{opt}$: (a) d = 3 m, ω = 1.27 rad/s, and (b) d = 3.5 m, ω = 1.22 rad/s.

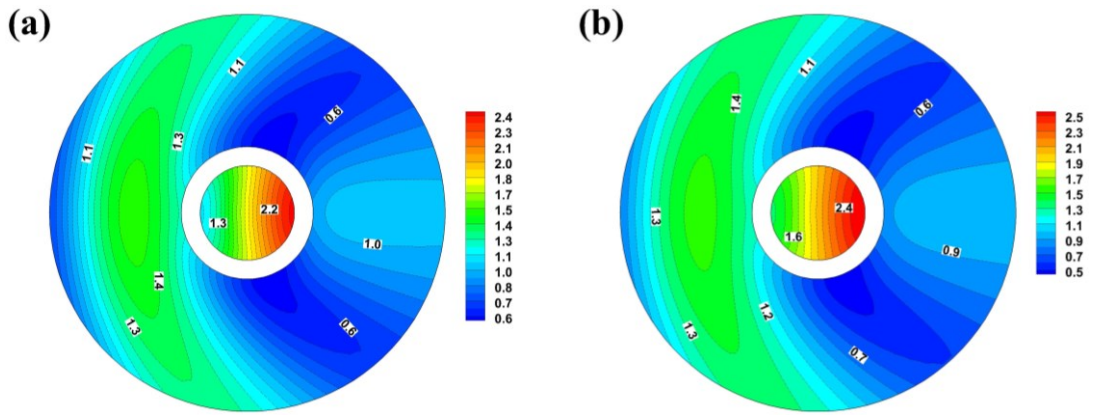

Fig. 18 Distribution of the free-surface elevation amplitude around free-floating OWCs with a = 5 m, b = 7 m, and $\chi = \chi_{opt}$: (a) d = 3.0 m, ω = 1.27 rad/s, and (b) d = 3.5 m, ω = 1.22 rad/s.

The variation of the transfer function of pressure-dependent radiation force and the wave excitation force for the heave motion is shown in Fig. 19. Due to the symmetry of the device, the pressure-dependent radiation force is zero for the anti-symmetric motion modes, i.e., surge and pitch. The wave excitation force for the heave motion generally decreases as the wave frequency increases due to the linear wave pressure decaying more rapidly along the vertical direction for shorter incident waves. The significant piston-mode motion of an internal fluid can enhance the wave forces for symmetric motion modes. The curves in Fig. 19 show obvious peaks around the resonance frequency of piston motion. In Fig. 20, apparent peaks can be found around the resonance frequency of heave motion. However, around the locations of the piston resonances, the enhancement of heave motion is much less pronounced. This phenomenon has been thoroughly explained in McIver (2005) and Konispoliatis and Mavrakos (2019), which is mainly owing to effect of the restoring force for a freely floating body.

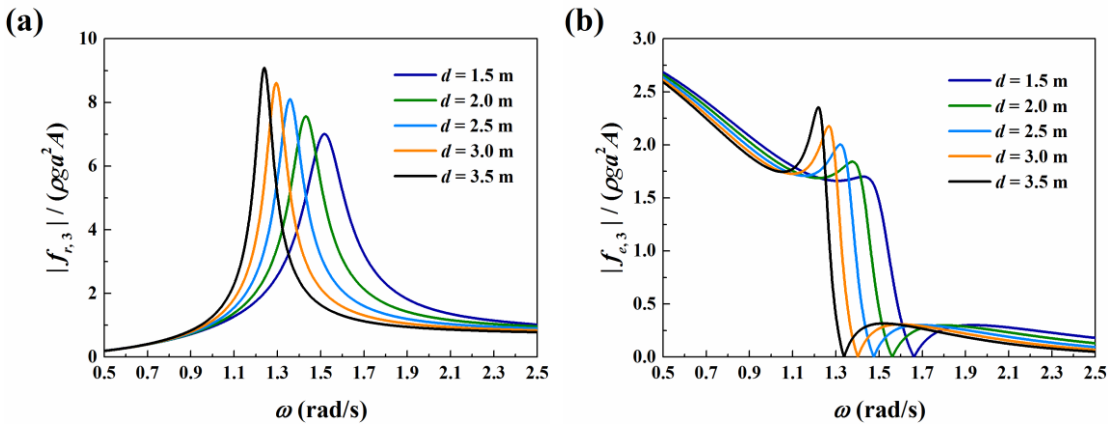

Fig. 19 Variation of the transfer function of vertical pressure-dependent radiation force and the vertical wave exciting force on cylindrical OWCs with a = 5 m, and b = 7 m for different drafts: (a) $L_{R,3}$, and (b) $f_{e,3}$

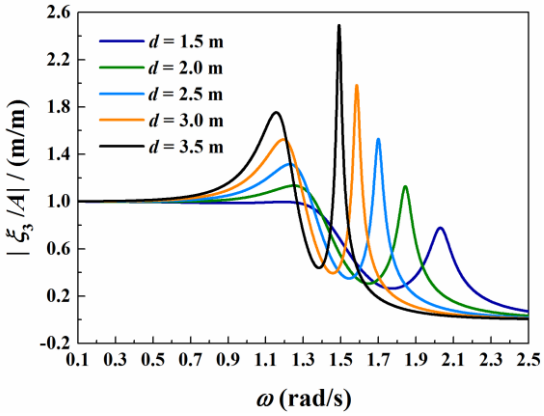

Fig. 20 Variation of heave motion amplitude of cylindrical OWCs with a = 5 m, and b = 7 m for different drafts

7.2.2 Wave power absorption of free-floating cylindrical OWCs

The results of air volume flux, oscillating air pressure, wave power absorption, and energy extraction efficiency are shown in Fig. 21. Here, the energy extraction efficiency E_c is defined as the ratio between the absorbed wave energy and the wave power of free incident waves passing through the width of 2a over a wave period. The airflow within a free-floating device depends on both the movement of the internal fluid and the body motion. Therefore, as shown in Fig. 21, the wave power absorption and energy extraction efficiency are all characterised by two apparent peaks. One is associated with the resonant piston-mode fluid motion, and the other is attained around the resonance frequency of heave motion. In addition, the air volume flux and oscillating air pressure enhancement can also be observed around these two specific frequencies.

The effect of the turbine parameter on the wave power absorption is illustrated in Fig. 22. At each wave frequency, the maximum wave energy absorption is attained when $\chi = \chi_{opt}$. A deviation from the optimal parameter reduces the wave power absorption and gradually narrows down the effective frequency bandwidth.

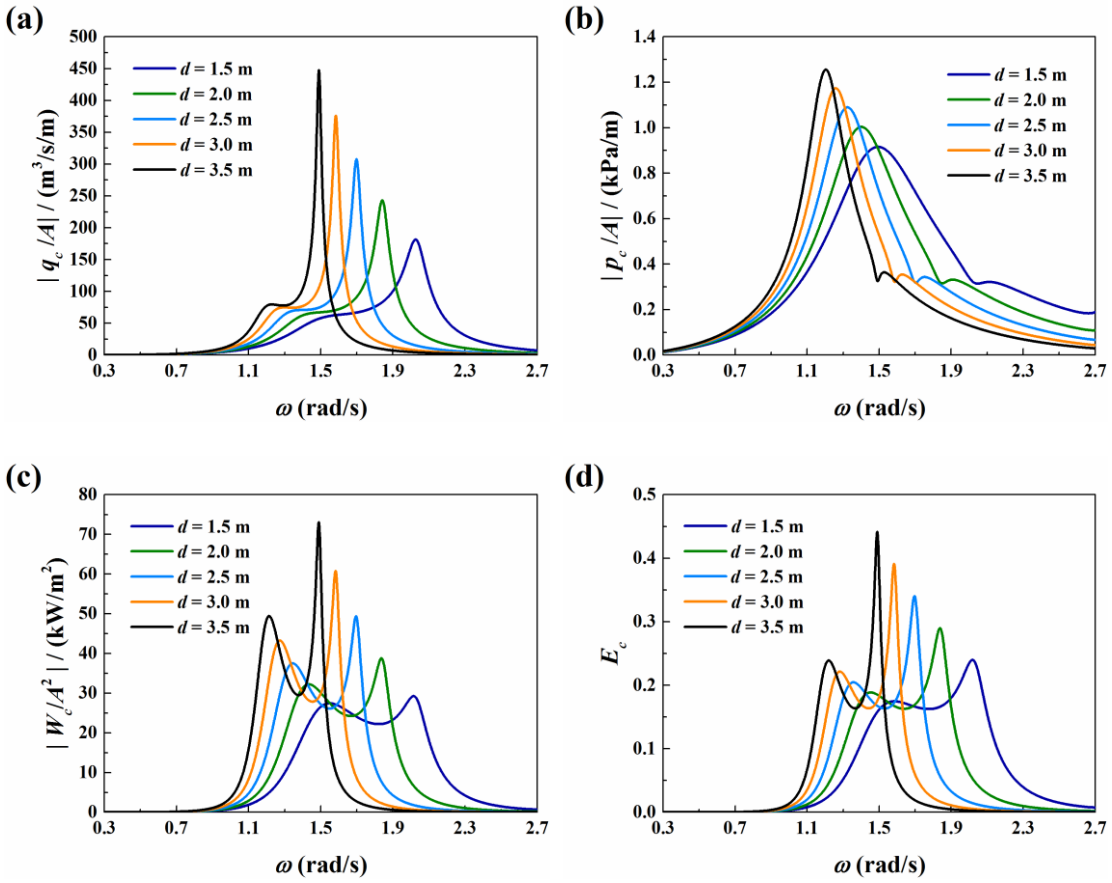

Fig. 21 Variation of the air volume flux, oscillating air pressure, wave power absorption extraction, and energy extraction efficiency of cylindrical OWCs with $a = 5$ m, $b = 7$ m, and $\chi = \chi_{opt}$ for different drafts: (a) Q_c, (b) P_c, (c) W_c, and (d) E_c

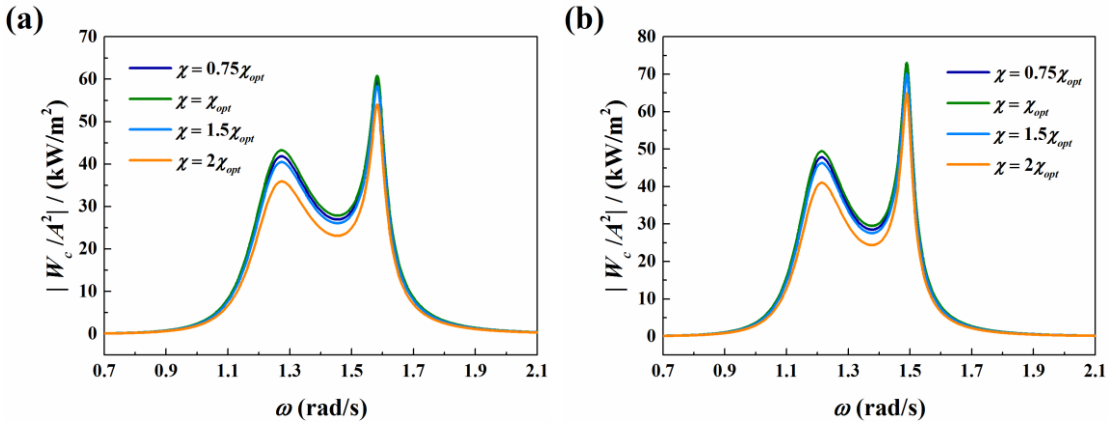

Fig. 22 Variation of the wave power absorption of cylindrical OWCs with $a = 5$ m, and $b = 7$ m for different turbine parameters: (a) $d = 3.0$ m, and (b) $d = 3.5$ m

679

680 **7.2.3 Mean wave drift force on floating cylindrical OWC devices**

681 Fig. 23 shows the results of the mean wave drift force and its constituent components
682 on stationary cylindrical OWCs. As discussed in the preceding sections, the mean wave
683 drift force on OWCs consists of both a term related to the far-field quantities and a term
684 associated with the oscillating air pressure over the internal free surface. As shown in
685 Fig. 23, the mean wave drift force on stationary cylindrical OWCs is mainly contributed
686 by the first term $f^{-}_{f,x}$. Due to the symmetry of the internal free surface and the uniform
687 distribution of the oscillating air pressure, the latter term $f^{-}_{n,x}$ is mainly caused by the
688 anti-symmetric mode of fluid motion. Therefore, noticeable enhancement of $f^{-}_{n,x}$ can
689 be observed around the locations of the sloshing resonances.

690 Analogous results with those in Fig. 23 but for free-floating devices are depicted in
691 Fig. 24. In Fig. 24, the mean wave drift force is generally dominated by $f^{-}_{f,x}$ over the
692 whole frequency region. Compared with stationary devices, the resonant sloshing
693 motion within the chamber is much less evident for free-floating ones, attributed to the
694 disturbance of radiation waves. As a result, apparent enhancement of $f^{-}_{n,x}$ at specific
695 wave frequencies cannot be observed from the results of free-floating devices.

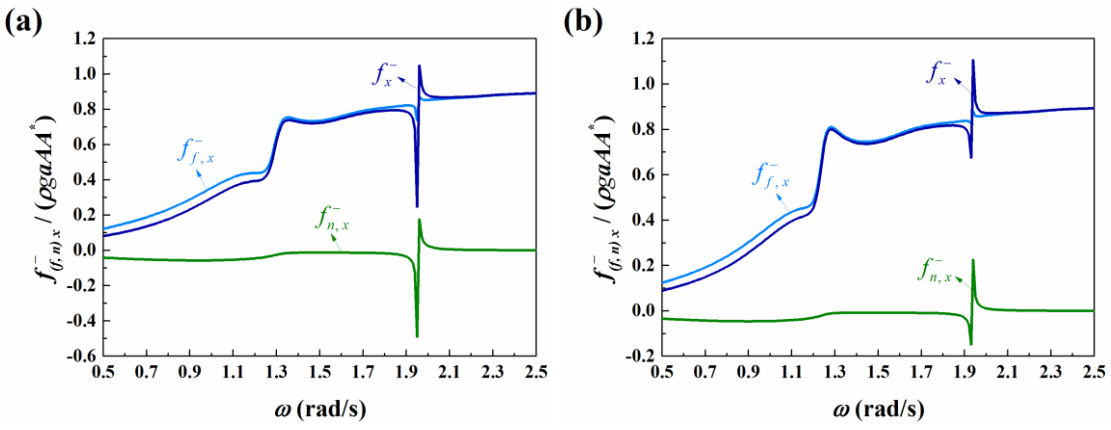

696

697 Fig. 23 Mean wave drift force and its constituent components on stationary cylindrical OWCs with
698 a = 5 m, b = 7 m, and $\chi = \chi_{opt}$: (a) d = 3.0 m, and (b) d = 3.5 m

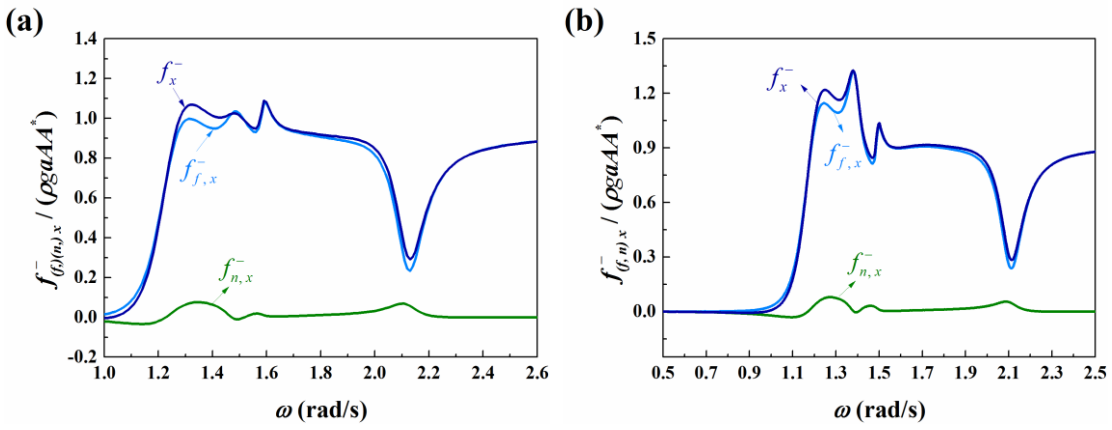

Fig. 24 Mean wave drift force and its constituent components on free-floating cylindrical OWCs with a = 5 m, b = 7 m, and $\chi = \chi_{opt}$: (a) d = 3.0 m, and (b) d = 3.5 m

7.3 Floating cylindrical OWCs with an arc-shaped reflector

To improve the device's performance, the geometry is optimised. The experimental study in Suroso (2005) showed that applying a reflector at the rear bottom can improve the efficiency of the OWC. In view of this, cylindrical OWC devices with an attached reflector (see Fig. 25) are considered in this section. As shown in Fig. 26, the arc-shaped plates are used as the reflector. It is of height l, thickness e, and attached at the rear bottom. The volume occupied by the reflector is defined by $a \le r \le a + e$, $-\alpha \le \theta \le \alpha$, and $-(d + l) \le z \le -d$. In the calculation, the height and thickness of the reflector are set as l = 3 m and e = 0.1 m, respectively. The draft of the cylindrical OWC is d = 3 m. Expressions of the coefficients in the mass and the hydrostatic restoring matrix are given in the Appendix.

In this section, the effect of the attached reflector on body motions and wave power absorption is primarily concerned. Other quantities are not discussed here for brevity. Fig. 27 shows the mesh discretisation used in the computation. In addition, due to the lack of restoring force, external stiffness is introduced to the surge motion by defining

$$K_{11} = C_k \cdot \left[\rho g \pi \left(b^2 - a^2 \right) \right], \tag{69}$$

where C_k is the ratio between the external stiffness in surge and the hydrostatic restoring stiffness in heave. Moreover, according to Sheng (2019), the following definition is made for the structural damping for surge motion:

$$B_{11} = 2 \cdot C_l \cdot \sqrt{|m + a_{11}| \cdot (K_{11} + c_{11})}, \tag{70}$$

where C_l is the linear damping ratio.

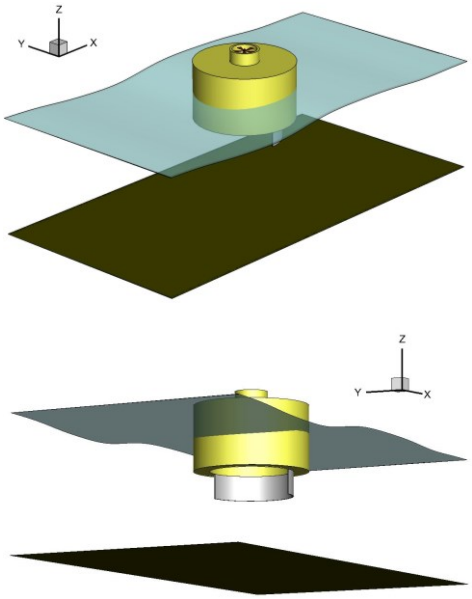

Fig. 25 Sketch of a floating cylindrical OWC with an attached arc-shaped reflector

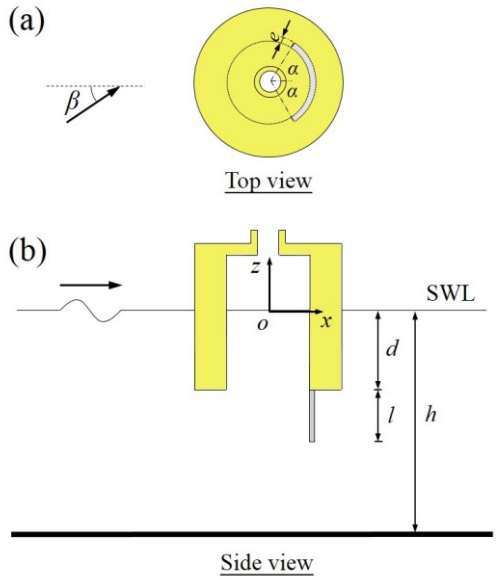

Fig. 26 Definition of the coordinate system for a floating cylindrical OWC with an attached arc-shaped reflector

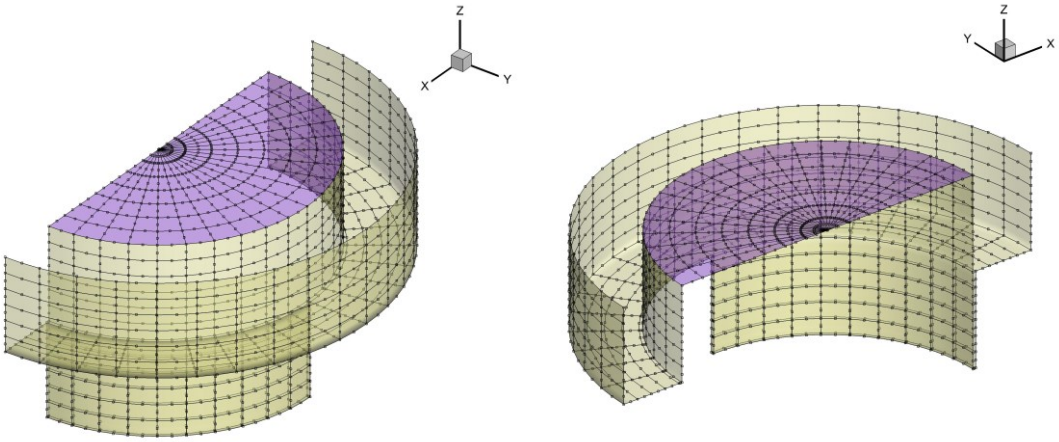

Fig. 27 Mesh discretisation in a half area for the computational case of a floating cylindrical OWC with an attached arc-shaped reflector

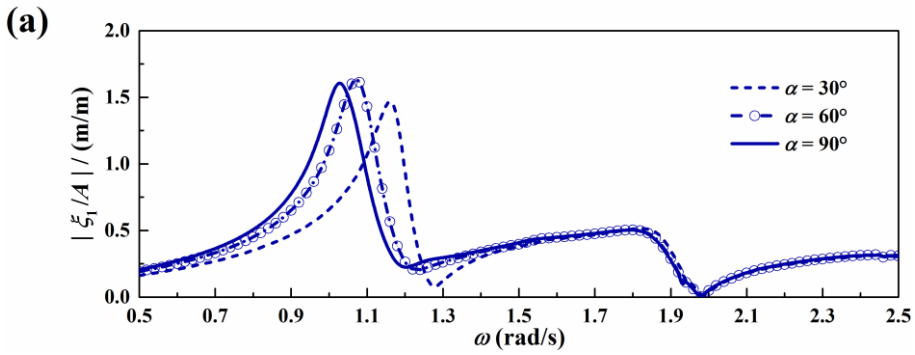

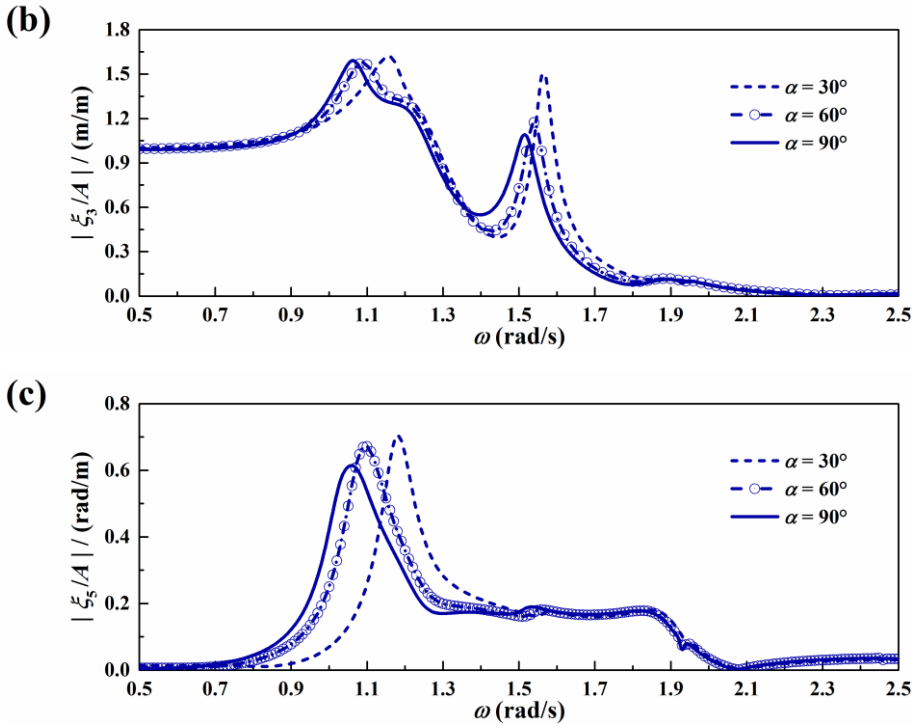

Fig. 28 Amplitude of surge, heave and pitch motions of a cylindrical OWC with an attached reflector with a = 5 m, b = 7 m, d = 3 m, h = 20 m, $\chi = \chi_{opt}$, C_l = 0.06, C_k = 2, and β = 0° for different plate sizes: (a) Surge, (b) heave, and (c) pitch.

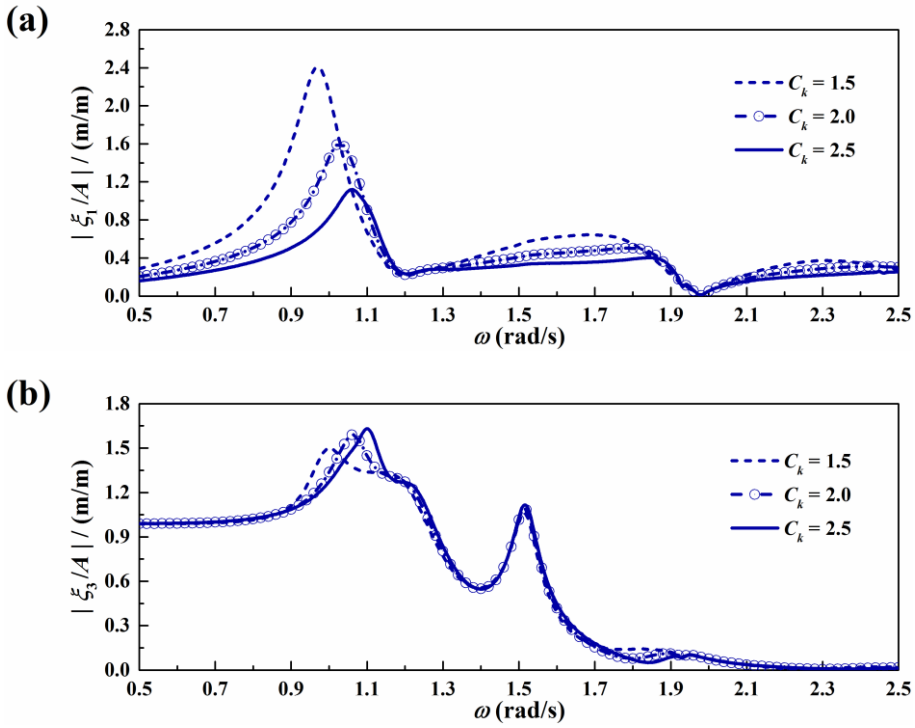

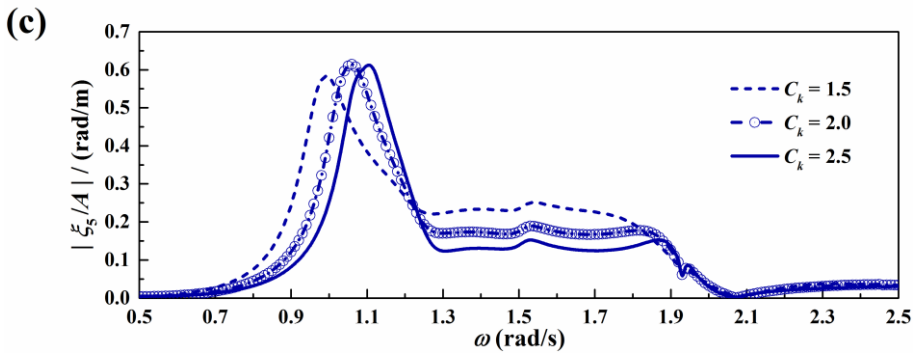

Fig. 29 Amplitude of surge, heave and pitch motions of a cylindrical OWC with an attached reflector with $a = 5$ m, $b = 7$ m, $d = 3$ m, $h = 20$ m, $\chi = \chi_{opt}$, $C_l = 0.06$, $\alpha = 90°$, and $\beta = 0°$ for different external stiffness: (a) Surge, (b) heave, and (c) pitch.

The surge, heave, and pitch motions for devices with an attached reflector are illustrated in Figs. 28 and 29, respectively, for different plate sizes and external stiffness. The significant peak of the surge motion at the location of resonance gradually moves to the high-frequency region with the decrease of α or the increase of C_k. With the presence of the reflector, the device symmetry with respect to *oyz* plane no longer exists. The surge motion is coupled with the heave and pitch motions. The pronounced surge motion at the resonance frequency can obviously enhance the heave and pitch motions.

The wave power absorption of devices with different plate sizes is shown in Fig. 30. As the plate size increases, the reflector can be more effective in preventing wave transmission and enhancing the wave energy that the device can absorb. As a result, in Fig. 30, the predominant peak gets more apparent as α increases.

A comparison between the wave energy harvesting of the devices with and without the reflector is illustrated in Fig. 31. In Fig. 31, ω_{heave} and ω_{piston} are used to denote the resonance frequencies of the heave motion and internal piston motion, respectively, for cylindrical OWCs; while, $\omega^{p}_{\text{surge}}$ and $\omega^{p}_{\text{heave}}$ are used to denote the resonance frequencies of the surge and heave motion, respectively, when with the reflector. With the reflector used, not only the heave but also the surge and pitch motions can excite the piston-mode fluid motion within the chamber and contribute to the air volume flux. As a result, the wave power absorption is characterised by a series of peaks. They can be observed around the resonance frequencies of the surge and heave motions. The

obvious peaks are also attained between ω = 1.17 rad/s and 1.31 rad/s, which are the resonance frequencies of the internal piston motion and the pitch motion, respectively, when with the reflector. The multiple modes of body motion are located over a wide frequency range, expanding the frequency bandwidth of efficient conversion. When the reflector is removed, the surge and pitch motions have a negligible impact on wave energy harvesting. However, when with the reflector, a significant surge motion occurs to harvest a large amount of wave energy, enhancing the performance of the device.

The effect of the external stiffness on the performance of the device is also shown in Fig. 31. The frequency range of the significant internal fluid motion mainly depends on the geometry of the chamber and cannot be easily adjusted. When the device undergoes multiple modes of body motion, the motions can enhance the air volume flux within the chamber and widen the frequency range in which the device performs well. Fig. 31 also illustrates that adjusting the external stiffness can be an effective way to tune the frequency range of high efficiency to a specified frequency region to harvest more energy, which is beneficial to the improvement of the device's adaptability to variable oceanic environments.

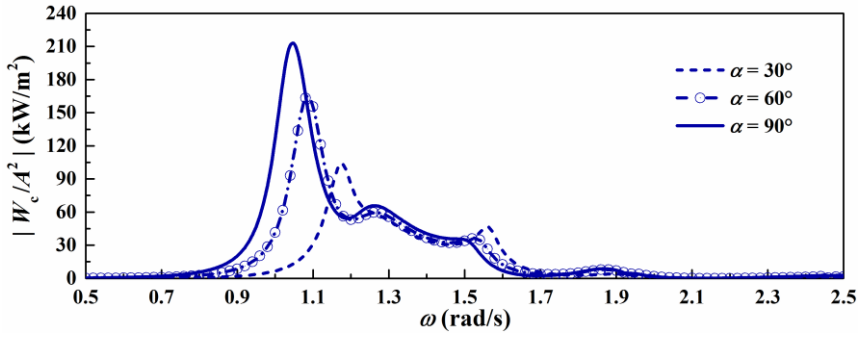

Fig. 30 Wave power absorption of a cylindrical OWC with an attached reflector with a = 5 m, b = 7 m, d = 3 m, h = 20 m, $\chi = \chi_{opt}$, C_l = 0.06, and β = 0° for different plate sizes

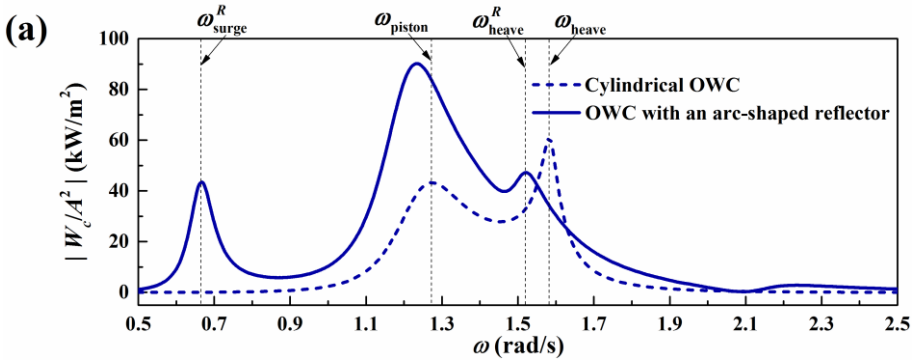

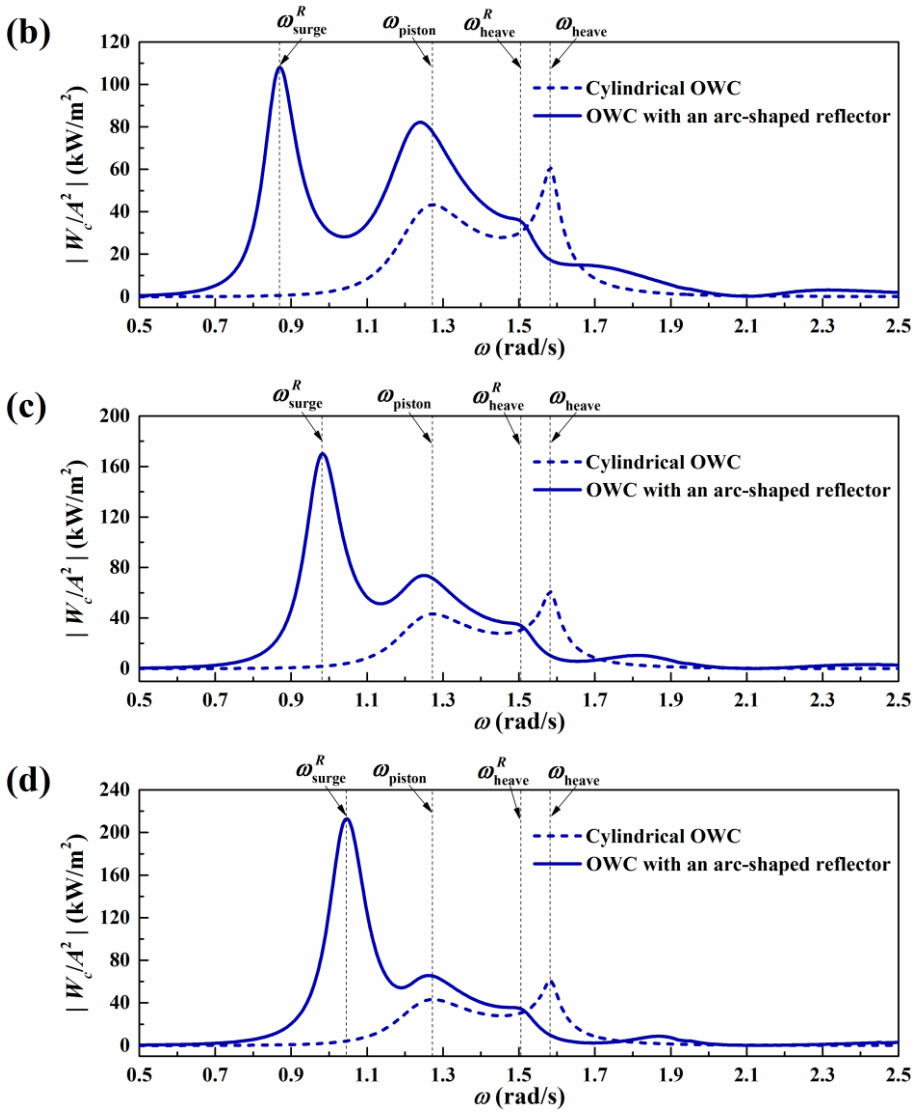

Fig. 31 A comparison of the wave power absorption of cylindrical OWCs with and without an attached reflector (a = 5 m, b = 7 m, d = 3 m, h = 20 m, $\chi = \chi_{opt}$, C_l = 0.06, and β = 0°): (a) C_k = 0.5, (b) C_k = 1.0, (c) C_k = 1.5, and (d) C_k = 2.0.

7.4 Floating cylindrical OWC on a submerged caisson

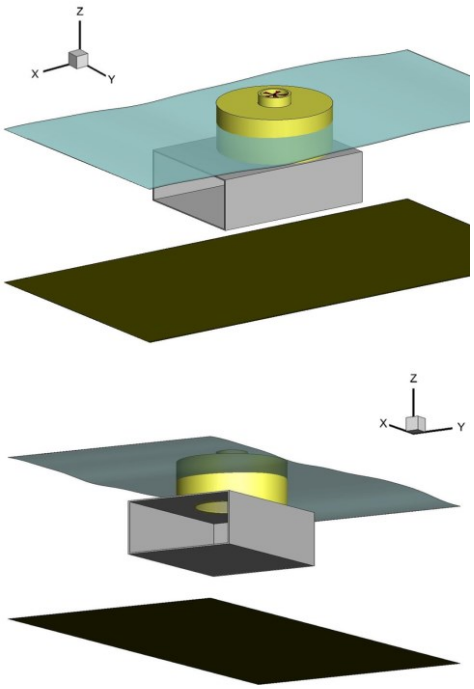

Fig. 32 Sketch of a floating cylindrical OWC on a submerged caisson

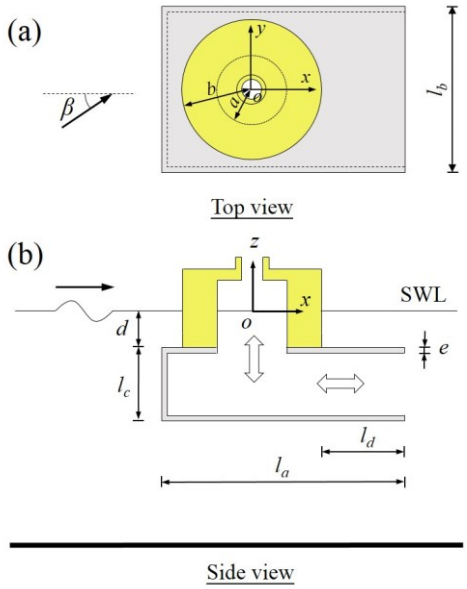

Fig. 33 Definition of the coordinate system for a floating cylindrical OWC on a submerged caisson and the definition of coordinate system

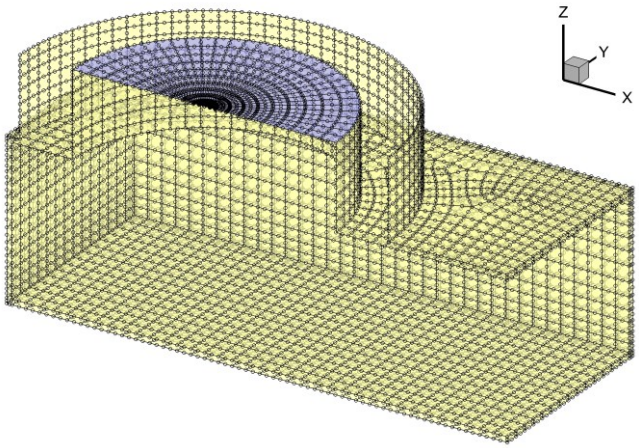

Fig. 34 Mesh discretisation in a half area for the computational case of a floating cylindrical OWC located on a submerged caisson

We then consider the cases where cylindrical OWC devices are located on a submerged caisson. As shown in Fig. 32, the caisson is attached rigidly at the bottom of the OWC. It is of length L_a, width L_b and height L_c, and composed of rigid plates with thickness e. The entire system has an "L" shape and is analogous to the BBDB type OWC device. A Cartesian coordinate system is shown in Fig. 33. The origin of the coordinate system is at the centre of the internal free surface. The x-axis points to the duct opening direction, and the z-axis points up positively. In the calculation, the

structural parameters of the caisson are set as $l_a = 19$ m, $l_b = 15$ m, $l_c = 6$ m, $l_d = 4.5$ m, and $e = 0.2$ m. In addition, the draft of the cylindrical OWC is $d = 3$ m. The mass of the whole device is 3.922×10^5 kg, and the radii of gyration about the x-, y- and z-axis are 5.188 m, 4.803 m, and 4.529 m, respectively.

The motion and the wave energy harvesting of the system are investigated. Fig. 34 shows the mesh discretisation used in the computation. The external stiffness and structural damping are introduced to the surge motion, determined according to Eqs. (69) and (70), respectively. In addition, structural damping has also been introduced to the heave and pitch motions. They are defined by

$$B_{33} = 2\cdot C_l \cdot \sqrt{\left|m + a_{33}\right| \cdot \left(K_{33} + c_{33}\right)}; \tag{71a}$$

$$B_{55} = 2\cdot C_l \cdot \sqrt{\left|m + a_{55}\right| \cdot \left(K_{55} + c_{55}\right)}. \tag{71b}$$

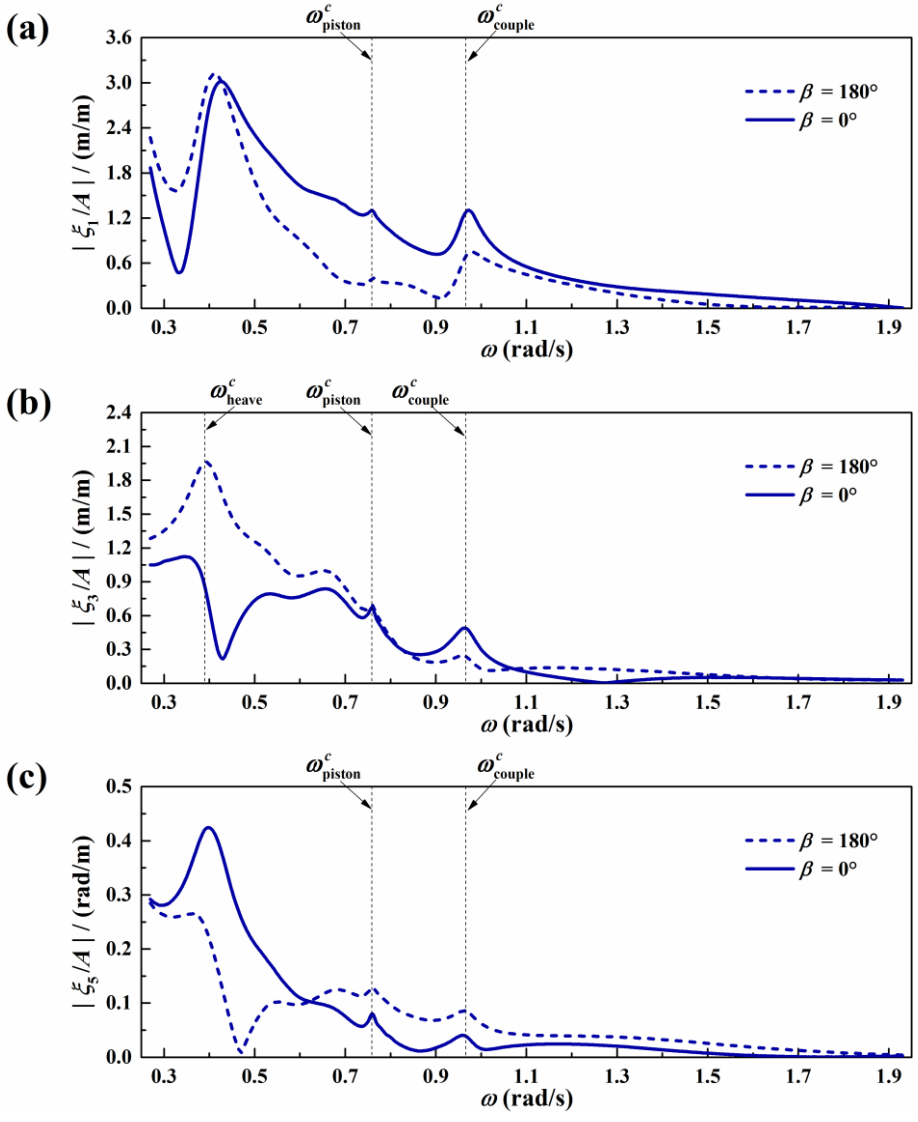

Fig. 35 Amplitudes of surge, heave and pitch motion of a cylindrical OWC located on a submerged caisson with a = 5 m, b = 7 m, d = 3 m, l_a = 19 m, l_b = 15 m, l_c = 6 m, l_d = 4.5 m, e = 0.2 m, h = 20 m, $\chi = \chi_{opt}$, C_k = 0.2, and C_l = 0.06: (a) surge, (b) heave, and (c) pitch

Fig. 35 shows the surge, heave and pitch motion amplitudes of the system with the caisson opening to the direction downstream ($\beta = 0°$) and upstream ($\beta = 180°$) the wave propagation, respectively. For the BBDB device, ω^c_{piston} and ω^c_{heave} are used to denote the resonance frequencies of the piston-mode fluid motion in the chamber and the heave motion of the device, respectively. In addition, ω^c_{couple} is used to denote the frequency where the significant coupling between the fluid motion in the caisson and the rigid-body motion occurs. C_k = 0.2 is applied in the computation, giving a loose restraint in the surge direction. External stiffness has not been applied to heave and pitch. The small stiffness and the relatively high inertia lead to the low-frequency resonant frequencies for surge and pitch motions, respectively. The heave motion with β = 180° is more apparent than that with β = 0° in the relatively low-frequency region and attains a predominant peak in the neighbourhood of ω^c_{heave} = 0.39 rad/s. When the cylindrical OWC rides on a submerged caisson, the piston-mode fluid motion in the chamber depends not only on the heave motion of the device but also on the surge and pitch motions. The surge and pitch motions can drive the airflow across the duct to cause a dynamic air force, which can, in turn, affect the heave motion. This causes the evident coupling between the fluid movement in the chamber and the body motion. Hence, different modes of body motion can be evidently enhanced in close proximity to ω^c_{piston} = 0.76 rad/s. The body motion and the fluid motion in the cylindrical chamber can also be affected by the movement of the fluid in the caisson. When the fluid in the caisson moves obviously in the horizontal plane and behaves like a rigid body, the whole device can then be approximated by a two-body system, in which the entrapped fluid is treated as a virtual rigid body and connected to the device hull by a damped stiffness. Due to the coupling effect of the two-body system, the apparent fluid motion in the caisson gives rise to the apparent enhancement of the body motion around ω^c_{couple} = 0.97 rad/s.

A comparison between the wave energy harvesting of the device with $\beta = 0°$ and $\beta = 180°$ is the shown in Fig. 36. When the caisson is opening to the direction upstream ($\beta = 180°$) the wave propagation, a portion of incident waves can travel into the caisson without any diffraction, which may enhance the energy absorption by the device. As a result, the case with $\beta = 180°$ generally owns a better performance at relatively low frequencies. With the increase of the wave frequency, the fluid velocity decays more quickly along the vertical direction, and it gets more difficult for the device to harvest energy directly from the waves. The body motion can then impose a more significant impact on the wave energy harvesting. Therefore, as the wave frequency grows further, especially when exceeding ω^c_{piston}, the case with $\beta = 0°$ has an apparently larger amount of energy absorption than that with $\beta = 180°$, which can be attributed to the larger surge motion of the former case. At ω^c_{piston}, the obvious peak with $\beta = 0°$ is much more remarkable than that with $\beta = 180°$. In Fig. 36, results for cylindrical devices, i.e., the submerged caisson is removed from the BBDB, have also been given for the direct comparison. The comparison shows that the presence of the caisson can remarkably improve the performance of the device over almost the entire frequency band.

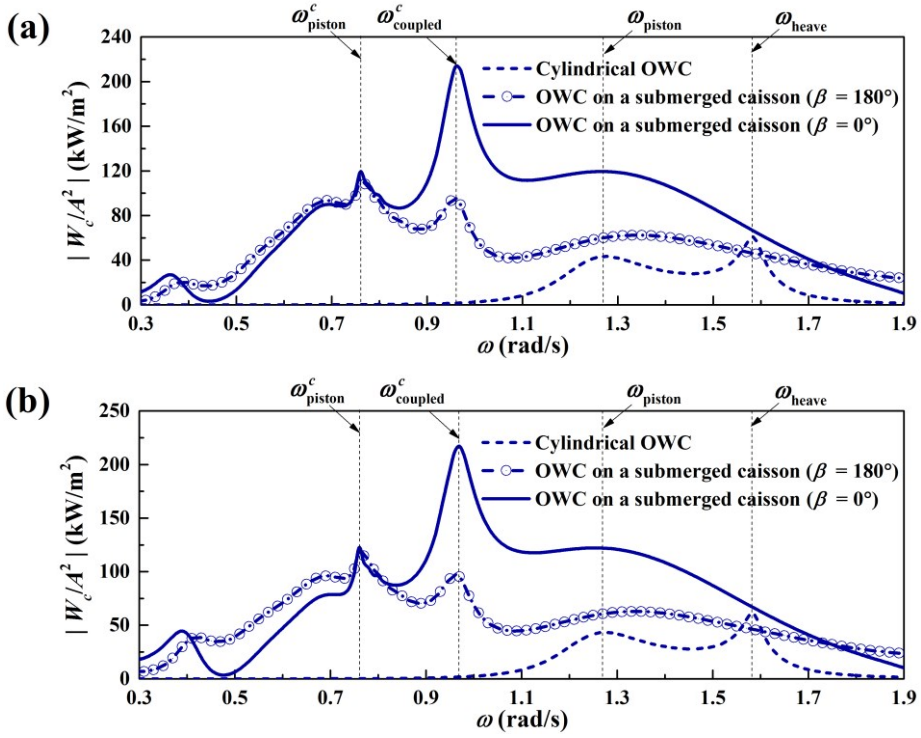

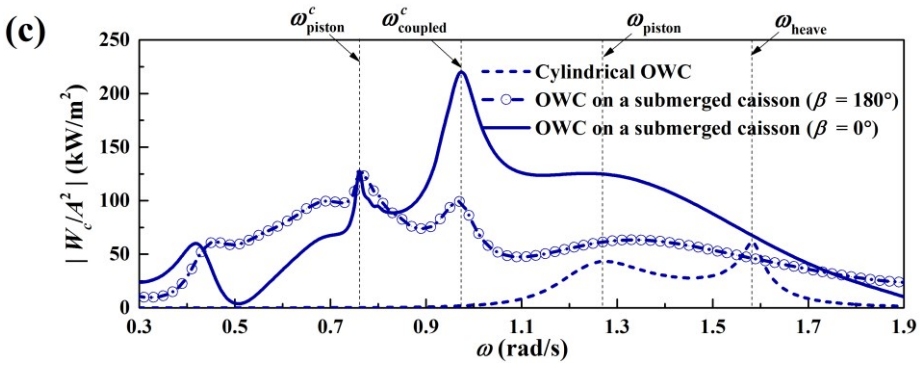

Fig. 36 Wave power absorption of a cylindrical OWC with and without an attached caisson (a = 5 m, b = 7 m, d = 3 m, l_a = 19 m, l_b = 15 m, l_c = 6 m, l_d = 4.5 m, e = 0.2 m, h = 20 m, $\chi = \chi_{opt}$, and C_l = 0.06): (a) C_k = 0.1, (b) C_k = 0.2, and (c) C_k = 0.3.

8. Conclusions

A numerical methodology has been developed in this study for the hydrodynamic analysis of arbitrarily shaped three-dimensional floating OWCs, including linear and nonlinear wave force, motion response, and wave power absorption. After confirming the validity of the developed method, detailed numerical studies are then conducted. The main conclusions are summarised as follows:

1) Typical free-surface oscillation modes, such as sloshing and piston, in the chamber of cylindrical OWCs are discussed. The resonant sloshing and piston motion of internal fluid causes the rapid variation of the hydrodynamic coefficients and wave forces for anti-symmetric (surge and pitch) and symmetric (heave) motion modes, respectively. When the device is free to move, the radiation waves can cause a breakdown of the resonant motion modes.

2) An optimal turbine parameter is derived for arbitrarily shaped three-dimensional OWCs undergoing coupled rigid-body motions. A deviation from the optimal parameter leads to the responding decrease of the wave energy harvesting and narrows down the effective frequency bandwidth.

3) The nonlinear mean wave drift force on OWCs is calculated based on momentum conservation. The derived formulation consists of two terms contributed from quantities at far-field and associated with the oscillating air pressure over the internal free surface, respectively. For stationary cylindrical OWCs, the second term can be evidently enhanced around the resonance frequency of the internal sloshing motion. However,

when the device is free to move, the resonant sloshing motion gets much less apparent due to the disturbance of radiation waves. Then, the entire force is dominated by the first term, while the second term maintains a small magnitude.

4) Two apparent peaks characterise the wave power absorption of free-floating cylindrical OWCs. One is associated with the resonant piston-mode fluid motion, and the other is in the location of the resonant heave motion. For cylindrical OWCs, the anti-symmetric motion modes, i.e., surge and pitch, are coupled. However, they are independent of the heave motion and piston-mode fluid motion.

5) Optimisation of the geometry has been made by attaching an arc-shaped reflector or locating the OWC on a submerged caisson. Attaching an arc-shaped reflector at the rear bottom can prevent wave transmission and enhance the internal fluid motion. With the presence of the reflector, the surge motion significantly impacts the wave energy harvesting. A significant surge motion occurs to harvest a large amount of wave energy. When a cylindrical OWC is located on a submerged caisson, the whole system is analogous to the BBDB type OWC device. Compared with a cylindrical OWC, a larger amount of wave energy can be entrapped and then absorbed by the device. The presence of the submerged caisson can remarkably improve the device's performance over almost the whole frequency region.

6) By attaching an arc-shaped reflector to the rear bottom or locating the device on a submerged caisson, the different rigid-body motions are coupled with each other, and they are also coupled with the OWC's resonance. A series of significant peaks characterise the wave energy harvesting. They are not only associated with the resonant motion of the entrapped fluid but also in close proximity to the resonance frequencies of the rigid-body motions, i.e., surge, heave, or pitch. Multiple peaks of the wave energy harvesting are located over a wide frequency range, which can expand the bandwidth of efficient conversion. In the meantime, the frequency range of the high efficiency can be tuned by adjusting the stiffness, etc., which improves the device's adaptability to the variable oceanic environments.

Acknowledgments

The work is financially supported by the National Natural Science Foundation of China (Grant Nos. 51809037, 51879039).

Appendix: Expression of the coefficients in the mass and restoring force matrix for a floating cylindrical OWC with an attached arc-shaped reflector

A floating cylindrical OWC with an attached arc-shaped reflector (see Figs. 25 and 26) is concerned. The cylindrical OWC is of inner radius a, outer radius b, and draft d. The attached reflector occupies a volume defined by $a \le r \le a + e$, $-\alpha \le \theta \le \alpha$, and $-(d + l) \le z \le -d$. The following assumptions have been made for the mass distribution of the system: 1) the submerged part accounts for the total mass of the device; 2) the mass is evenly distributed over the submerged part.

The displacement and mass of the system, defined as V_b and m_b, respectively, are expressed as

$$V_b = S_1 d + S_2 l. \tag{A1a}$$

$$m_b = \rho V_b, \tag{A1a}$$

where

$$S_1 = \pi\left(b^2 - a^2\right); \tag{A2a}$$

$$S_2 = \alpha\left[\left(a+e\right)^2 - a^2\right]. \tag{A2b}$$

The mass centre $\mathbf{x}_c$ coincides with the buoyancy centre $\mathbf{x}_b$. That is

$$x_b = x_c = \frac{2l\left[\left(a+e\right)^3 - a^3\right]\sin\alpha}{3V_b}; \tag{A3a}$$

$$y_b = y_c = 0; \tag{A3b}$$

$$z_b = z_c = -\frac{d^2 S_1 + \left[\left(d+l\right)^2 - d^2\right]S_2}{2V_b}. \tag{A3c}$$

Then, the expression of the coefficients in the mass matrix is given by:

$$m_{11} = m_b; \quad m_{15} = m_b z_c; \quad m_{1l} = 0, \ \left(l = 2,\ 3,\ 4,\ 6\right); \tag{A4a}$$

$$m_{22} = m_b; \quad m_{24} = -m_b z_c; \quad m_{26} = m_b x_c; \quad m_{2l} = 0, \ \left(l = 1,\ 3,\ 5\right); \tag{A4b}$$

$$m_{33}=m_b;\quad m_{35}=-m_b x_c;\quad m_{3l}=0,\ (l=1,\ 2,\ 4,\ 6); \tag{A4c}$$

$$m_{42}=-m_b z_c;\quad m_{44}=I_{22}^b+I_{33}^b;\quad m_{46}=-I_{13}^b,\quad m_{4l}=0,\ (l=1,\ 3,\ 5); \tag{A4d}$$

$$m_{51}=m_b z_c;\quad m_{53}=-m_b x_c;\quad m_{55}=I_{11}^b+I_{33}^b,\quad m_{5l}=0,\ (l=2,\ 4,\ 6); \tag{A4e}$$

$$m_{62}=m_b x_c;\quad m_{64}=-I_{13}^b;\quad m_{66}=I_{11}^b+I_{22}^b,\quad m_{6l}=0,\ (l=1,\ 3,\ 5). \tag{A4f}$$

The parameters I_{11}^b, I_{22}^b, I_{33}^b and I_{13}^b in Eq. (A4) are defined by

$$I_{11}^b=\frac{1}{4}\rho d\pi\left(b^4-a^4\right)+\frac{1}{8}\rho l\left(2\alpha+\sin 2\alpha\right)\left[(a+e)^4-a^4\right]; \tag{A5a}$$

$$I_{22}^b=\frac{1}{4}\rho d\pi\left(b^4-a^4\right)+\frac{1}{8}\rho l\left(2\alpha-\sin 2\alpha\right)\left[(a+e)^4-a^4\right]; \tag{A5b}$$

$$I_{33}^b=\frac{1}{3}\rho d^3 S_1+\frac{1}{3}\rho\left[(d+l)^3-d^3\right]S_2; \tag{A5c}$$

$$I_{13}^b=-\frac{\rho}{2}\left[(d+l)^2-d^2\right]\left\{\frac{2\sin\alpha}{3}\left[(a+e)^3-a^3\right]\right\}. \tag{A5d}$$

In addition, the coefficients in the hydrostatic restoring force matrix is given by following expression:

$$c_{1l}=0,\ (l=1,\ 2,\ ...,\ 6); \tag{A6a}$$

$$c_{2l}=0,\ (l=1,\ 2,\ ...,\ 6); \tag{A6b}$$

$$c_{33}=\rho g\pi\left(b^2-a^2\right),\quad c_{3l}=0\ (l=1,\ 2,\ 4,\ 5,\ 6); \tag{A6c}$$

$$c_{44}=\frac{1}{4}\rho g\pi\left(b^4-a^4\right),\quad c_{4l}=0\ (l=1,\ 2,\ 3,\ 5,\ 6); \tag{A6d}$$

$$c_{55}=\frac{1}{4}\rho g\pi\left(b^4-a^4\right),\quad c_{5l}=0\ (l=1,\ 2,\ 3,\ 4,\ 6); \tag{A6e}$$

$$c_{6l}=0,\ (l=1,\ 2,\ ...,\ 6). \tag{A6f}$$

When l or α is set as zero, the expressions in Eqs. (A1) to (A5) are reduced to those for a cylindrical OWC.

Reference

[1] Cruz J. Ocean Wave Energy. 2008, Springer, Berlin, Heidelberg, Germany.

[2] Cong P W, Gou Y, Teng B. A new approach to low-frequency QTF and its application in predicting slow drift force. Ocean engineering, 2012, 53: 25-37.

[3] Cong P W, Bai W, Teng B, Gou Y. Semi-analytical solution to the second-order wave loads on a

vertical cylinder in bi-chromatic bi-directional waves. Ocean Engineering, 2018, 161: 205-220.

[4] Cong P W, Teng B, Bai W, Ning D Z, Liu Y Y. Wave power absorption by an oscillating water column (OWC) device of annular cross-section in a combined wind-wave energy system. Applied Ocean Research, 2021, 107: 102499.

[5] Choi Y R, Hong S Y, Choi H S. An analysis of second-order wave forces on floating bodies by using a higher-order boundary element method. Ocean Engineering, 2001, 28(1): 117-138.

[6] Deng Z Z, Huang Z H, Law A W K. Wave power extraction by an axisymmetric oscillating-water-column converter supported by a coaxial tube-sector-shaped structure. Applied Ocean Research, 2013, 42: 114-123.

[7] Eatock Taylor R, Huang J B. Semi-analytical formulation for second-order diffraction by a vertical cylinder in bichromatic waves. Journal of fluids and structures, 1997, 11(5): 465-484.

[8] Evans D V, Porter R. Efficient calculation of hydrodynamic properties of OWC-Type devices. Journal of Offshore Mechanics and Arctic Engineering, 1997, 119(4): 210-218.

[9] Elhanafi A, Macfarlane G, Fleming A, Leong Z. Experimental and numerical investigations on the intact and damage survivability of a floating–moored oscillating water column device. Applied Ocean Research, 2017, 68: 276-292.

[10] Falnes J, Mciver P. Surface wave interactions with systems of oscillating bodies and pressure distributions. Applied Ocean Research, 1985, 7(4): 225-234.

[11] Falnes J. Ocean waves and oscillating systems. Cambridge University Press, 2002.

[12] Falcão A F O. Wave energy utilization: A review of the technologies. Renewable and Sustainable Energy Reviews, 2010, 14(3): 899-918.

[13] Falcão A F O, Henriques J C C. Oscillating-water-column wave energy converters and air turbines: A review. Renewable Energy, 2016, 85: 1391-1424.

[14] Gomes R P F, Henriques J C C, Gato L M C, AFO Falcão. Hydrodynamic optimization of an axisymmetric floating oscillating water column for wave energy conversion. Renewable Energy, 2012, 44: 328-339.

[15] Gielen D, Boshell F, Saygin D, Bazilian M D, Wagner N, Gorini R. The role of renewable energy in the global energy transformation. Energy Strategy Reviews, 2019, 24: 38-50.

[16] Gomes R P F, Henriques J C C, Gato L M C, Falcão A F O. Wave power extraction of a heaving floating oscillating water column in a wave channel. Renewable Energy, 2016, 99: 1262-1275.

[17] Gadelho J F M, Rezanejad K, Xu S, Hinostroza M, Guedes Soares C. Experimental study on the motions of a dual chamber floating oscillating water column device. Renewable Energy, 2021, 170: 1257-1274.

[18] Hong D C, Hong S Y, Hong S W. Numerical study of the motions and drift force of a floating OWC device. Ocean Engineering, 2004, 31(2): 139-164.

[19] Heath T V. A review of oscillating water columns. Philosophical Transactions of the Royal Society London, Series A: Mathematical, Physical and Engineering Sciences, 2012, 370(1959): 235-245.

[20] He F, Huang Z, Law A W K. An experimental study of a floating breakwater with asymmetric pneumatic chambers for wave energy extraction. Applied energy, 2013, 106: 222-231.

[21] He F, Leng J, Zhao X Z. An experimental investigation into the wave power extraction of a floating box-type breakwater with dual pneumatic chambers. Applied Ocean Research, 2017, 67: 21-30.

[22] Heo K, Kashiwagi M. Numerical study on the second-order hydrodynamic force and response of an elastic body–In bichromatic waves. Ocean Engineering, 2020, 217: 107870.

[23] Kashiwagi M, Endo K, Yamaguchi H. Wave drift forces and moments on two ships arranged side by side in waves. Ocean engineering, 2005, 32(5-6): 529-555.

[24] Kim M H, Yue D K P. The complete second-order diffraction solution for an axisymmetric body Part 2. Bichromatic incident waves and body motions. Journal of Fluid Mechanics, 1990, 211: 557-593.

[25] Konispoliatis D N, Mavrakos S A. Hydrodynamic analysis of an array of interacting free-floating oscillating water column (OWC's) devices. Ocean Engineering, 2016, 111: 179-197.

[26] Konispoliatis D N, Mavrakos S A. Natural frequencies of vertical cylindrical oscillating water column devices. Applied Ocean Research, 2019, 91: 101894.

[27] Ledoux A, Molin B, Delhommeau G, Fabien Remy. A Lagally formulation of the wave drift force. In Proceedings of the 21st International Workshop Water Waves and Floating Bodies, 2006, Loughborough, United Kingdom.

[28] Luo Y Y, Nader J R, Cooper P, et al. Nonlinear 2D analysis of the efficiency of fixed oscillating water column wave energy converters. Renewable energy, 2014a, 64: 255-265.

[29] Luo Y Y, Wang Z W, Peng G J, Xiao Y X, Zhai L M, Liu X Zhang Q. Numerical simulation of

a heave-only floating OWC (oscillating water column) device. Energy, 2014b, 76: 799-806.

[30] McIver P, Evans D V. The occurrence of negative added mass in free-surface problems involving submerged oscillating bodies. Journal of engineering mathematics, 1984, 18(1): 7-22.

[31] McIver. Complex resonances in the water – wave problem for a floating structure. Journal Fluid Mechanics, 2005, 536: 423–443

[32] Mei C C, Stiassnie M, Yue D K P. Theory and applications of ocean surface waves. Singapore: World Scientific, 2005.

[33] Michele S, Renzi E, Perez-Collazo C, Greaves D, Iglesias G. Power extraction in regular and random waves from an OWC in hybrid wind-wave energy systems. Ocean Engineering, 2019, 191: 106519.

[34] Mavrakos S A. Wave loads on a stationary floating bottomless cylindrical body with finite wall thickness. Applied Ocean Research, 1985, 7(4): 213-224.

[35] Martins-Rivas, H, Mei C C. Wave power extraction from an oscillating water column at the tip of a breakwater. Journal of Fluid Mechanics, 2009, 626: 395-414.

[36] Nader J R, Zhu S P, Cooper P, Stappenbelt B. A finite-element study of the efficiency of arrays of oscillating water column wave energy converters. Ocean Engineering, 2012, 43: 72-81.

[37] Nihous G C. Wave power extraction by arbitrary arrays of non-diffracting oscillating water columns. Ocean Engineering, 2012, 51: 94-105.

[38] Ning D Z, Zhou Y, Zhang C W. Hydrodynamic modeling of a novel dual-chamber OWC wave energy converter. Applied Ocean Research, 2018, 78:180-191.

[39] Newman J N. Second-order slowly-varying forces on vessels in irregular waves. In: Proceedings of the International Symposium on the Dynamics of Marine Vehicles on Structures in Waves, University College London, London, 1974.

[40] Newman J N, Lee C H. Boundary-element methods in offshore structure analysis. Journal of Offshore Mechanics and Arctic Engineering, 2002, 124(2): 81-89.

[41] Rezanejad K, Bhattacharjee J, Guedes Soares C. Analytical and numerical study of dual-chamber oscillating water columns on stepped bottom. Renewable Energy, 2015, 75: 272-282.

[42] Sarmento A J N A, Falcão A F O. Wave generation by an oscillating surface-pressure and its application in wave-energy extraction. Journal of Fluid Mechanics, 1985, 150: 467-485.

[43] Suroso A. Hydraulic model test of wave energy conversion. Jurnal Mekanikal, 2005, 19: 84-

94.

[44] Shao Y L. Numerical analysis of second-order mean wave forces by a stabilized higher-order boundary element method. 37th International Conference on Ocean, Offshore and Arctic Engineering, Madrid, Spain, 17-22 July, 2018.

[45] Shao Y L, Zheng Z P, Liang H, Chen J K. A consistent second-order hydrodynamic model in the time domain for floating structures with large horizontal motions. Computer-Aided Civil and Infrastructure Engineering, 2022, 37: 894-914.

[46] Sheng W A. Motion and performance of BBDB OWC wave energy converters: I, hydrodynamics. Renewable energy, 2019, 138: 106-120.

[47] Teng B, Eatock Taylor R. New higher-order boundary element method for wave diffraction/radiation. Applied Ocean Research, 1995, 17(2): 71-77.

[48] Teng B, Cong P W. A novel decomposition of the quadratic transfer function (QTF) for the time-domain simulation of non-linear wave forces on floating bodies. Applied Ocean Research, 2017, 65: 112-128.

[49] Vijayakrishna Rapaka E, Natarajan R, Neelamani S. Experimental investigation on the dynamic response of a moored wave energy device under regular sea waves. Ocean Engineering, 2004, 31(5): 725-743.

[50] Vyzikas T, Deshoulières S, Barton M, Ciroux O, Greaves D, Simmonds D. Experimental investigation of different geometries of fixed oscillating water column devices. Renewable Energy, 2017, 104: 248-258.

[51] Yeung R W, Wang L. Radiation and exciting forces of axisymmetric structures with a moonpool in waves. Journal of Marine Science and Application, 2018, 17(3): 297-311.

[52] Wang C, Deng Z Z, Wang P J, Yao Y. Wave power extraction from a dual oscillating-water-column system composed of heave-only and onshore units. Energies, 2019, 12(9): 1742.

[53] Wang C, Zhang Y Y, Deng Z Z. Semi-analytical study on the wave power extraction of a bottom-seated oscillating water column device with a pitching front lip-wall. Journal of Fluids and Structures, 2021, 105: 103350.

[54] Zheng S M, Zhang Y L, Iglesias G. Wave–structure interaction in hybrid wave farms. Journal of Fluids and Structures, 2018, 83: 386-412.

[55] Zheng S M, Antonini A, Zhang Y L, Greaves D, Miles J. Wave power extraction from multiple

oscillating water columns along a straight coast. Journal of Fluid Mechanics, 2019, 878: 445-480.

[56] Zhu G X, Graham D, Zheng S M, Hughes J, Greaves D. Hydrodynamics of onshore oscillating water column devices: A numerical study using smoothed particle hydrodynamics. Ocean Engineering, 2020, 218: 108226.

[57] Zhao X L, Zhang L, Li M W, Johanning L. Experimental investigation on the hydrodynamic performance of a multi-chamber OWC-breakwater. Renewable and Sustainable Energy Reviews, 2021, 150: 111512.